Time-dependent probability density functions, information geometry and entropy production in a stochastic prey–predator model of fusion plasmas

Patrick Fuller ✉ iD ; Eun-jin Kim iD ; Rainer Hollerbach iD ; Bogdan Hnat

Check for updates

CrossMark

View Online

Export Citation

Time-dependent probability density functions, information geometry and entropy production in a stochastic prey–predator model of fusion plasmas

Patrick Fuller,[1,2,a] (iD) Eun-jin Kim,[1] (iD) Rainer Hollerbach,[3] (iD) and Bogdan Hnat[2]

AFFILIATIONS

[1]Fluid and Complex Systems Research Centre, Coventry University, Coventry CV1 2TT, United Kingdom
[2]Department of Physics, University of Warwick, Coventry CV4 7AL, United Kingdom
[3]Department of Applied Mathematics, University of Leeds, Leeds LS2 9JT, United Kingdom

[a]Author to whom correspondence should be addressed: Patrick.Fuller@warwick.ac.uk

ABSTRACT

A stochastic, prey–predator model of the L–H transition in fusion plasma is investigated. The model concerns the regulation of turbulence by zonal and mean flow shear. Independent delta-correlated Gaussian stochastic noises are used to construct Langevin equations for the amplitudes of turbulence and zonal flow shear. We then find numerical solutions of the equivalent Fokker–Planck equation for the time-dependent joint probability distribution of these quantities. We extend the earlier studies [Kim and Hollerbach, Phys. Rev. Res. **2**, 023077 (2020) and Hollerbach et al., Phys. Plasmas **27**, 102301 (2020)] by applying different functional forms of the time-dependent external heating (input power), which is increased and then decreased in a symmetric fashion to study hysteresis. The hysteresis is examined through the probability distribution and statistical measures, which include information geometry and entropy. We find strongly non-Gaussian probability distributions with bi-modality being a persistent feature across the input powers; the information length to be a better indicator of distance to equilibrium than the total entropy. Both dithering transitions and direct L-–H transitions are (also) seen when the input power is stepped in time. By increasing the number of steps, we see less hysteresis (in the statistical measures) and a reduced probability of H-mode access; intermittent zonal flow shear is seen to have a role in the initial suppression of turbulence by zonal flow shear and stronger excitation of intermittent zonal flow shear for a faster changing input power.

I. INTRODUCTION

The L–H transition[1] is a non-equilibrium phenomenon observed in magnetic confinement fusion (MCF) plasmas where a significant improvement in plasma confinement is reached once an external power exceeds a certain threshold. It is accompanied by the decrease in turbulence due to sheared poloidal flows.[2–4] Due to the improvement in confinement, H-mode is important to the future of fusion reactors as a preferred mode of operation for power generation. For instance in ITER, H-mode is a basic operating scenario and the auxiliary heating power needs to be sufficient to allow H-mode to be reached.[5,6]

In the MCF plasma, the background density and temperature gradients are sources of free energy, which are vulnerable to linear and non-

linear instabilities. Linear instabilities, such as interchange and drift-wave, harness the free energy and lead to turbulent fluctuations. Turbulence excites poloidal flows via the Reynolds stress, these are known as zonal flows. Mean poloidal flows are driven by the background ion pressure gradient. Both zonal and mean flows are radially sheared and suppress turbulence by shearing turbulent eddies, providing a mechanism for controlling the turbulence level.[7,8] It has been established for some time that intermittent turbulent transport at the plasma edge is of fundamental importance for controlled confinement of plasmas in toroidal devices.[9–13] The transport events can occur at a range of temporal and spatial scales including large (device) scale events.[14]

There has been work to develop statistical models of intermittency in turbulence using a variety of turbulence models. These

include ion temperature gradient (ITG) turbulence where the probability distribution function (PDF) for the ion heat flux has been numerically computed and found to have enhanced exponential tails.[15–17] The probability distribution for the local Reynolds stress in forced Hasegawa-Mima turbulence has been calculated analytically and also found to have a stretched tail.[18] These and other works have studied plasma turbulence using stationary PDFs, to study the non-equilibrium case a time-dependent PDF must be calculated. A time-dependent PDF has been calculated in the work presented in this paper to study the Low-to-High (L–H) transition in fusion plasmas, which is understood to be a non-equilibrium phenomenon.

Zero-dimensional models have been used to study the L–H transition using three ODE[19,20] and four ODE[21] systems. The models have a prey–predator paradigm and focus on the regulation of turbulent fluctuations (prey) by zonal and mean flow shear (predators). The system of equations used in Ref. 19 has been extended by including stochastic noise in the evolution equations for turbulence and zonal flow shear, which incorporates the effect of physics on much smaller temporal scales than the evolution of low frequency drift-like turbulence and large scale zonal and mean flows. The addition of Gaussian distributed noise to the dynamical equation means the turbulence drive has a random component, which is relevant to intermittent transport events. In our model turbulence and zonal flow shear are also driven by noise as well as terms from the deterministic model, an effect of this is lowering the power at which the L-H transition can occur. A discussion of the (constant) power threshold for the L-H transition in the deterministic and stochastic models can be found in the Appendix. The PDFs produced by the stochastic model in the previous work were often found to be strongly non-Gaussian, with an enhanced population of strong zonal flow shear suggesting intermittency in zonal flow shear is important in turbulence suppression. Information geometry diagnostics (see Sec. IV) were calculated from the PDFs which provided insight into the self-regulation between turbulence and zonal flow shear. In the remainder of this paper, mean flow shear and zonal flow shear will simply be referred to as mean flows and zonal flows respectively.

The work in this paper continues the work in Refs. 22 and 23, by using heating scenarios in which the input power is increased and then decreased in a symmetric fashion to study hysteresis. Both linear and step functions are used as the input power; the effect of the ramping rate (for the linear functions) and the effect of the number of steps (for the step functions) on the evolution of the PDF and diagnostics/statistical measures is what is investigated. The statistical measures are the information length and entropy (see Secs. IV and V), including the total entropy production.

II. MODEL

The model used in this work is the same model used in Refs. 22 and 23, a 0-dimensional (in space) deterministic prey–predator model[19] which has been extended to include stochastic noise. Self-organization of shear flows has been observed in reduced models and also in 2D hydrodynamic models,[24,25] suggesting self-organization is a phenomenon which is qualitatively reproduced across a variety of models. This property is employed here in the study of another reduced model which involves the self-organization of shear flows, and means our results have relevance to more sophisticated fluid models and experiments. Using a reduced model means the L–H transition

can be studied at relatively low computational cost while still allowing comparison with the results from higher dimensional (2D, 3D) fluid models and experiments.[2–4]

A. Deterministic model

The prey–predator model at the core of the work is given by

$$\frac{\partial \epsilon}{\partial t} = N\epsilon - a_1 \epsilon^2 - a_2 V^2 \epsilon - a_3 v^2 \epsilon, \tag{1}$$

$$\frac{\partial v}{\partial t} = b_1 \epsilon \frac{v}{1 + b_2 V^2} - b_3 v, \tag{2}$$

$$\frac{\partial N}{\partial t} = Q - c_1 \epsilon N - c_2 N. \tag{3}$$

The quantities are the turbulent fluctuation amplitude ($\epsilon \geq 0$), the zonal flow shear (v), the density gradient (N), the input power (Q), and the mean flow shear $V = dN^2$. The a_i, b_i, c_i, and d are non-negative constants. The first term on the right side of equation (1) represents the growth of turbulence, which is proportional to the background density gradient; the second term represents energy transfer due to the non-linear turbulence interaction; the third term represents damping due to the mean flow shear; and the fourth term represents damping due to the zonal flow shear. The first term on the right side of equation (2) represents the growth of zonal flows from turbulence which is subject to damping from mean flows; and the second term represents linear damping. The first term on the right side of equation (3) represents the growth of the density gradient from the input power; the second term represents damping due to turbulence; and the third term represents damping due to neo-classical affects.[26,27] The H-mode described by this model is a quiescent H-mode where $\epsilon = v = 0$.

B. Stochastic model

The purpose of extending the deterministic model is to incorporate the effects of smaller scale physics, which are not included in the mean-field model, as noted in the introduction. To construct the stochastic model from Eqs. (1)–(3), we use $x = \pm\sqrt{\epsilon}$ instead so that the boundary conditions can be specified at $x \to \pm\infty$. Equation (3) is also approximated by its stationary solution,

$$N = \frac{Q}{c_1 \epsilon + c_2}, \tag{4}$$

in order to reduce the computational cost of numerically solving a stochastic model. Independent δ-correlated Gaussian stochastic noises ξ and η are added, respectively, to Eqs. (1) and (2) to obtain out stochastic model,[28]

$$\frac{dx}{dt} = f + \xi, \quad f = \frac{1}{2}\left[N - a_1 x^2 - a_2 V^2 - a_3 v^2\right]x, \tag{5}$$

$$\frac{dv}{dt} = g + \eta, \quad g = \frac{b_1 x^2 v}{1 + b_2 V^2} - b_3 v. \tag{6}$$

The noise terms satisfy

$$\langle \xi(t)\xi(t')\rangle = 2D_x \delta(t - t'), \quad \langle \eta(t)\eta(t')\rangle = 2D_v \delta(t - t'), \\ \langle \xi(t)\eta(t')\rangle = 0, \quad \langle \xi \rangle = \langle \eta \rangle = 0, \tag{7}$$

where the angular brackets denote ensemble averages. D_x and D_v are the amplitudes of the stochastic noise ξ and η, respectively.

C. Fokker–Planck Equation

Instead of directly using Eqs. (5) and (6) in stochastic simulations, a Fokker–Planck equation[28] is derived using (5)–(7) and solved for a PDF $p(x, v, t)$,

$$\frac{\partial p}{\partial t} = -\frac{\partial}{\partial x}[f(x, v)p] - \frac{\partial}{\partial v}[g(x, v)p] + D_x \frac{\partial^2 p}{\partial x^2} + D_v \frac{\partial^2 p}{\partial v^2}. \quad (8)$$

Solving a Fokker–Planck (FP) equation for a PDF has the advantage of guaranteeing a smooth PDF, whereas a very large ensemble of stochastic dynamical runs would be needed to achieve such a solution. The PDF has boundary conditions such that $p(x, v, t) \rightarrow 0$ as $x, v \rightarrow \pm\infty$.

A finite difference scheme is used to numerically solve the FP equation. The spatial discretization is second-order accurate, a second-order Runge–Kutta method is used to time step the solution, and the x diffusion term is treated implicitly whereas all other terms are treated explicitly. The time step used is $\Delta t = 2.5 \times 10^{-5}$. The FP equation is only solved for positive x, v since (8) is invariant for $x \rightarrow -x$ and $v \rightarrow -v$. This results in substantial computational savings when running the code. The grid spacings in x and v are 10^{-3} with $x_{max} = v_{max} = 2$. These boundaries result in very good probability conservation, for all runs presented here the total probability is conserved to within 10^{-8}, four orders of magnitude better than in Ref. 23.

We use a parallelized version of the code previously used in Refs. 22 and 23. The parallelism is done by distributing the grid points in v across different processors, 48 processors were used to obtain the results in this paper. Such a parallelized code then allows far more thorough studies, on finer grids, than the previous code did.

III. INFORMATION LENGTH

One of the diagnostics used to study the system in this paper is the information length, $\mathcal{L}(t)$.[29,30] The information length is the cumulative change to a PDF along a path, a function of time only when the model and initial PDF parameters are fixed. It is derived from the relative entropy by considering two PDFs, which are temporally adjacent along an evolution path, $p(x, t)$ and $p(x, t + \delta t)$, and taking the limit $\delta t \rightarrow 0$. This defines the infinitesimal relative entropy $\mathcal{E}$ as

$$\mathcal{E} = \int dx dv \frac{1}{p(x, v, t)} \left[\frac{\partial p(x, v, t)}{\partial t} \right]^2, \quad (9)$$

for the joint PDF $p(x, v, t)$. Taking the square root of the infinitesimal relative entropy $\mathcal{E}$ defines the information rate $\Gamma = \sqrt{\mathcal{E}}$ which has units of time^{-1}. Summing the information rate along the path defines the information length $\mathcal{L}$ as

$$\mathcal{L}(t) = \int_0^t \Gamma(t_1) dt_1. \quad (10)$$

The information length can also be defined for the marginal PDFs $p(x, t)$ and $p(v, t)$,

$$\mathcal{E}_x = \int dx \frac{1}{p(x, t)} \left[\frac{\partial p(x, t)}{\partial t} \right]^2, \quad (11)$$

$$\mathcal{E}_v = \int dv \frac{1}{p(v, t)} \left[\frac{\partial p(v, t)}{\partial t} \right]^2, \quad (12)$$

$$\mathcal{L}_x(t) = \int_0^t \Gamma_x(t_1) dt_1, \quad \mathcal{L}_v(t) = \int_0^t \Gamma_v(t_1) dt_1, \quad (13)$$

where $\Gamma_x = \sqrt{\mathcal{E}_x}$ and $\Gamma_v = \sqrt{\mathcal{E}_v}$. For two independent variables x and v with $p(x, v, t) = p(x, t)p(v, t)$, $\mathcal{E}_x + \mathcal{E}_v = \mathcal{E}$.

The information rate is invariant under a time-independent change of variable, meaning Γ and Γ_x calculated from $p(x, v, t)$ and $p(x, t)$ are identical to Γ and Γ_ϵ calculated from $p(\epsilon, v, t)$ and $p(\epsilon, t)$. The information rates of different variables have the same unit (time^{-1}) and the information length is unitless, meaning they can be directly compared to examine any correlation between the variables, with self-regulation being of key interest.

IV. ENTROPY

The entropies associated with the joint PDF $p(x, v, t)$ and marginal PDFs $p(x, t)$ and $p(v, t)$ are defined using the following expressions:

$$S_x = -\int dx\, p(x, t) \ln(p(x, t)), \quad (14)$$

$$S_v = -\int dv\, p(v, t) \ln(p(v, t)), \quad (15)$$

$$S = -\int dx dv\, p(x, v, t) \ln(p(x, v, t)). \quad (16)$$

These expressions contain an implicit underlying measure which resolves the issues of dimensionality in taking the logarithm of a PDF. The entropy measures the disorder in the system, whose statistics is represented by the PDFs.[31] It should be noted that unlike the information length diagnostics, entropy is not invariant under the coordinate transformation $\epsilon \rightarrow x$ while it is invariant under a linear translation $x \rightarrow x + a$ for constant a, a problem since the L-H transition involves the movement of the PDF. These properties make entropy not particularly suited to our study; however, it will be included as a means of comparison with other diagnostics.

Differentiating S with respect to time allows for new expressions to be derived: $\dot{S} = \dot{S}_T - \dot{S}_m$, where $\dot{S}_T$ is the rate of total entropy production, which is non-negative by definition, and $\dot{S}_m$ is the entropy flux to environment. These are given by

$$\dot{S}_T = \int dx dv \left[\frac{J_x^2}{D_x p} + \frac{J_v^2}{D_v p} \right] = \dot{S}_{Tx} + \dot{S}_{Tv}, \quad (17)$$

$$\dot{S}_m = \int dx dv \left[\frac{J_x f}{D_x} + \frac{J_v g}{D_v} \right] = \dot{S}_{mx} + \dot{S}_{mv}, \quad (18)$$

where $J_x(x, v, t)$ is the x current density and $J_v(x, v, t)$ is the v current density. The total entropy production tells us how far from equilibrium the system is along the evolution path, since $\dot{S}_T = 0$ in an equilibrium reversible process. The entropy flux to the environment $\dot{S}_m$ is positive when entropy flows from the system to the environment and negative when entropy flows from the environment to the system.

V. RESULTS

The objective of this work is to investigate the effect of a variety of input powers on the evolution of the time-dependent PDFs and various diagnostics, with particular attention paid to H-mode access. All powers have been chosen to have an increasing stage (referred to in

the paper as the forward process) and a decreasing stage (referred to in the paper as the backward process), which are symmetric around a time t_*. The purpose of having forward and backward processes is to examine any asymmetry in the process upon the reversal of a symmetric power source. The asymmetry in the evolution of the PDF and diagnostics during the forward and backward processes is referred to as (dynamical) hysteresis in the paper. The exact choices of the input powers is as follows:

- Set 1: $Q = 0.03t + 0.1$, $t_* = 40$, $Q_{max} = 1.3$.
- Set 2: $Q = 0.01t + 0.1$, $t_* = 120$, $Q_{max} = 1.3$.
- Sets 3, 4, and 5: Step functions with differing numbers of steps, all reaching $Q_{max} = 1$. The specifics of the sets can be seen in Fig. 1.

Set 1 is the slowest ramping rate used in Ref. 23 and is used here to provide a comparison with the much slower ramping set 2, which is the same heating rate used in the deterministic model.[19] This will enable us to investigate the effect of stochastic noise in the deterministic model in.[19] In addition to sets 1–2, we also consider step changes in power which have previously not been investigated. Neutral beam input power is often stepped in practical experiments.[3,32] The consequence of different numbers of steps on the evolution of the system and hysteresis is investigated. Note that the total energy deposition from Q is the same for sets 3 and 5, and ∼20% larger for set 4. The energy deposition for sets 1 and 4 is also the same. All sets have similar maximum powers; $Q_{max} = 1.3$ for sets 1 and 2, and $Q_{max} = 1$ for sets 3, 4, and 5. Sets 3–5 have a lower maximum power than sets 1–2 due to H-mode solutions dominating in the steady state for a constant power of $Q = 1$ (see the Appendix). Therefore, we investigate the impact of reaching $Q_{max} = 1$ in one, two and three steps and maintaining this power for different lengths of time. The choice of $Q(t = 0) = 0.1$ instead of $Q(t = 0) = 0$ for the rampings is to reach the dithering stage quicker.

The exact parameters used to produce the results in this paper are as follows. The constants used in the model are $a_1 = 0.2$, $a_2 = a_3 = 0.7$, $b_1 = 1.5$, $b_2 = b_3 = 1$, $c_1 = 1$, $c_2 = 0.5$, and $d = 1$. These are the same values which were used in Ref. 19. The initial condition is a Gaussian centered on $(x, v) = (0.5, 0)$ with standard deviations $\sigma_x = \sigma_v = 0.05$. The noise amplitudes are $D_x = D_v = 10^{-4}$.

A. Joint and Marginal PDFs

1. Linear Q

Figure 2 shows the joint PDF $p(x, v, t)$ in the (x, v) plane at times $t = 10, 20, 30, \ldots, 80$ for set 1. The marginal PDFs p_x and p_v are shown in Figs. 3 and 4, respectively. The PDF shows a complex evolution over the sampled times. Initially there is the growth of zonal flows and subsequent self-regulation between turbulence and zonal flows (also known as dithering). This is followed by the growth of a secondary peak at the origin due to the suppression of turbulence and zonal flows by mean flows as the power increases. The formation of a bi-modal PDF with a peak at $x = v = 0$ and a peak at $x \sim 1$, $v \sim 0.7$ shows the coexistence of H-mode (in our model this is a quiescent H-mode characterized by $x = v = 0$[19]) and dithering (characterized by $x = v \neq 0$) solutions as the power is linearly increased and decreased. The marginal PDFs are strongly bi-modal. In terms of hysteresis, the maximum of the joint PDF occurs at $t = 51$ so does not coincide with the input power maximum at $t = 40$.

During the forward process the evolution of the PDF is dominated by a single peak. The position of this peak and the width of the distribution varies substantially. A secondary peak at the origin appears when the input power reaches approximately the value $Q = 1$. The peak at the origin continues to grow during the backward process, reaching a maximum at $t = 51$, and remains throughout the backward process, its width gradually increasing. The position of a second peak, away from the origin, is relatively constant until $t = 60$ and its width is decreasing.

The joint PDF $p(x, v, t)$ for set 2 is shown in Fig. 5 at times $t = 30, 60, 90, \ldots, 240$. The marginal PDFs p_x and p_v are shown in Figs. 6 and 7, respectively. Initially there is development of zonal flows which is followed by dithering; the single peak PDF is relatively stationary between $t = 50$ and $t = 90$. The initial dithering in set 1 is more exaggerated than in set 2 since a faster power ramping drives the system further from equilibrium. A bi-modal PDF forms with a highly concentrated peak at the origin which persists until it eventually recombines with the original peak. The peak which forms at the origin is larger for set 2 compared with set 1, showing the greater dominance of mean flows for the slower ramping, and there is greater separation of the magnitudes of the two peaks for set 2. When the peak at the
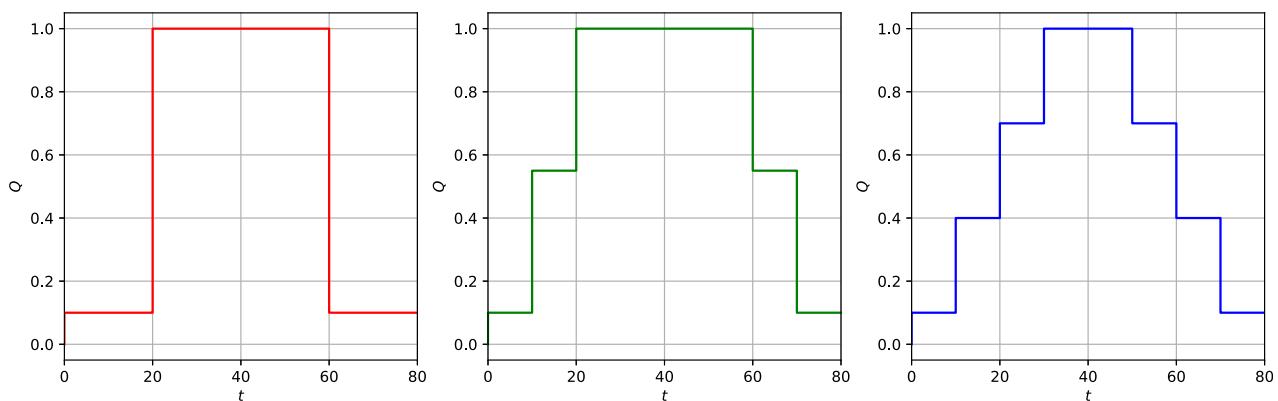

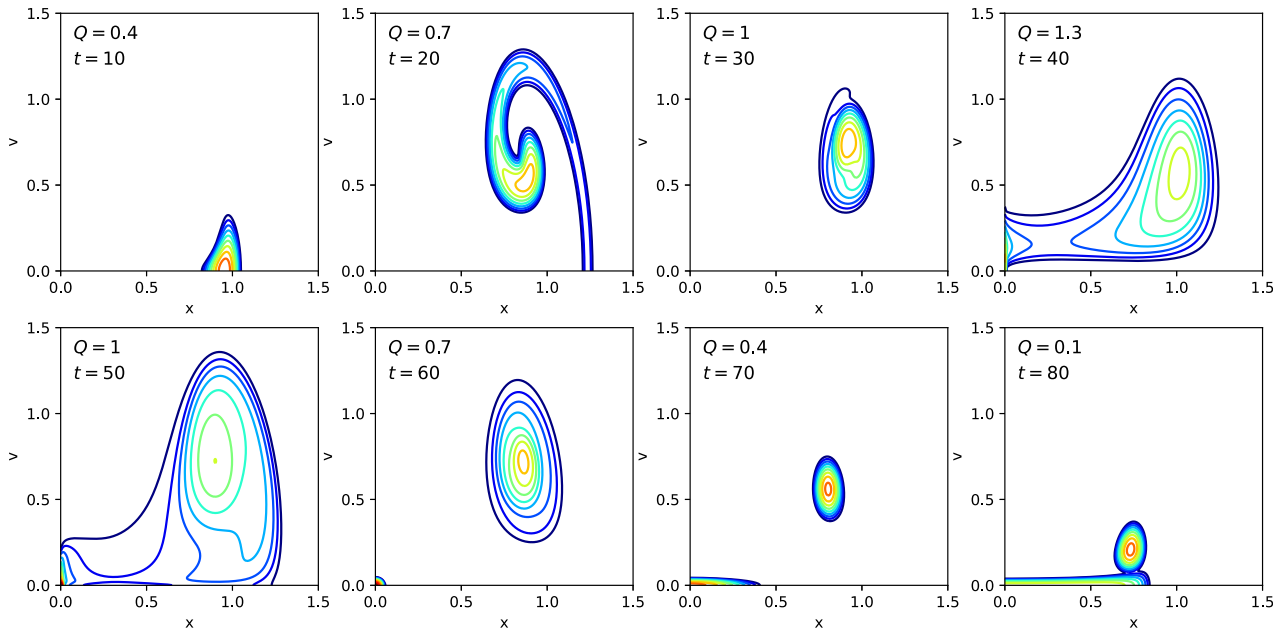**FIG. 1.** (left) Set 3, (middle) set 4, and (right) set 5.

FIG. 2. Contour plots of the joint PDF $p(x, v, t)$ for $D_x = D_v = 10^{-4}$ in the (x, v) plane for set 1. The plots are labeled with the instantaneous time (t) and power (Q). The contours are on a logarithmic scale, ranging from 10^{-2} to 10^3 with intervals of $10^{0.5}$.
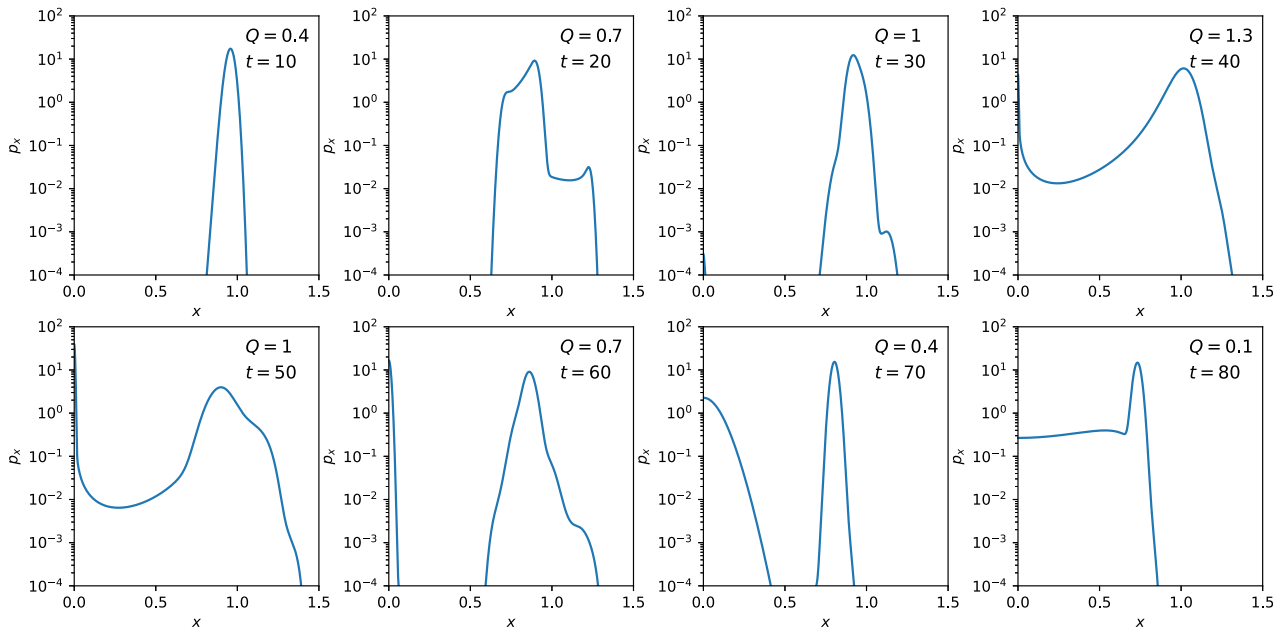

FIG. 3. The marginal PDF p_x for $D_x = D_v = 10^{-4}$ for set 1.

origin is maximum, for set 2 the original peak is ~0.006% its value, whereas for set 1, it is ~1%. The greater separation between the two peaks for set 2 can also be seen in the marginal PDFs. The hysteresis for set 2 is similar to that seen in set 1 in terms of the forward process being dominated by a single peak and the backward process being dominated by two peaks. The major differences consist of the PDF being more stationary in the forward process for set 2 and the weaker bi-modality for set 2. The maximum of the joint PDF occurs at $t = 132$, 12 units after the power maximum. Interestingly this is the same lag in absolute terms as for set 1. At t = 210, p_x is flat between
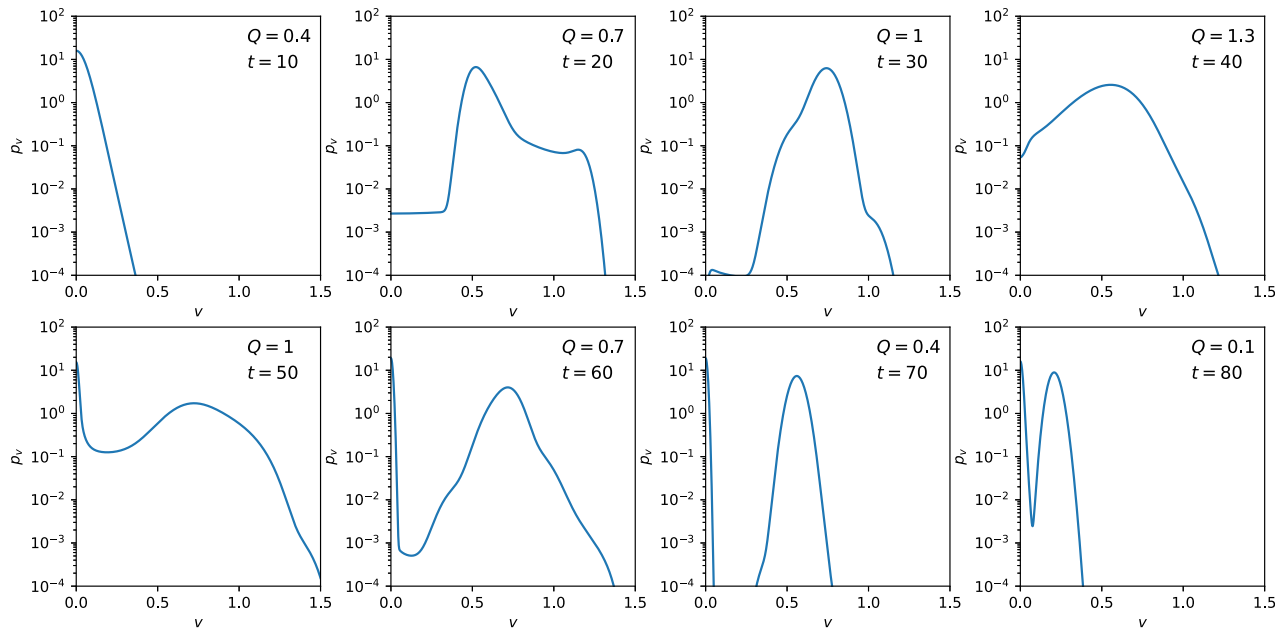
FIG. 4. The marginal PDF p_v for $D_x = D_v = 10^{-4}$ for set 1.
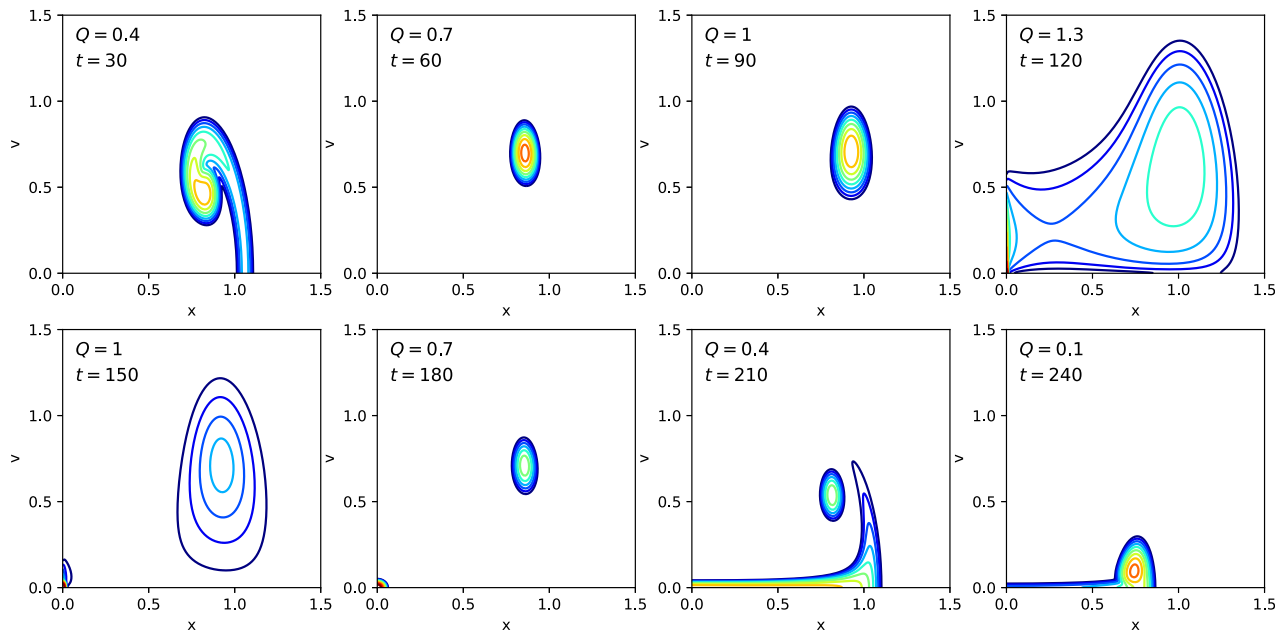

FIG. 5. Contour plots of the joint PDF $p(x, v, t)$ for $D_x = D_v = 10^{-4}$ in the (x, v) plane for set 2. The plots are labeled with the instantaneous time (t) and power (Q). The contours are on a logarithmic scale, ranging from 10^{-2} to 10^{3} with intervals of $10^{0.5}$.

$x = 0$ and $x \sim 1$ whilst for p_v the multi-peak structure with the dominant peak at $v = 0$ remains.

For set 1, at $t = 20$ the long right tail of p_v around the global maximum suggests a role of intermittent zonal flows in regulating the turbulence during the initial dithering stage. We can see in Fig. 7 that this feature is absent for set 2, suggesting intermittent zonal flows do not contribute as much to regulating turbulence in the initial dithering stage. Also, the larger peak which forms at the origin for set 2 suggests
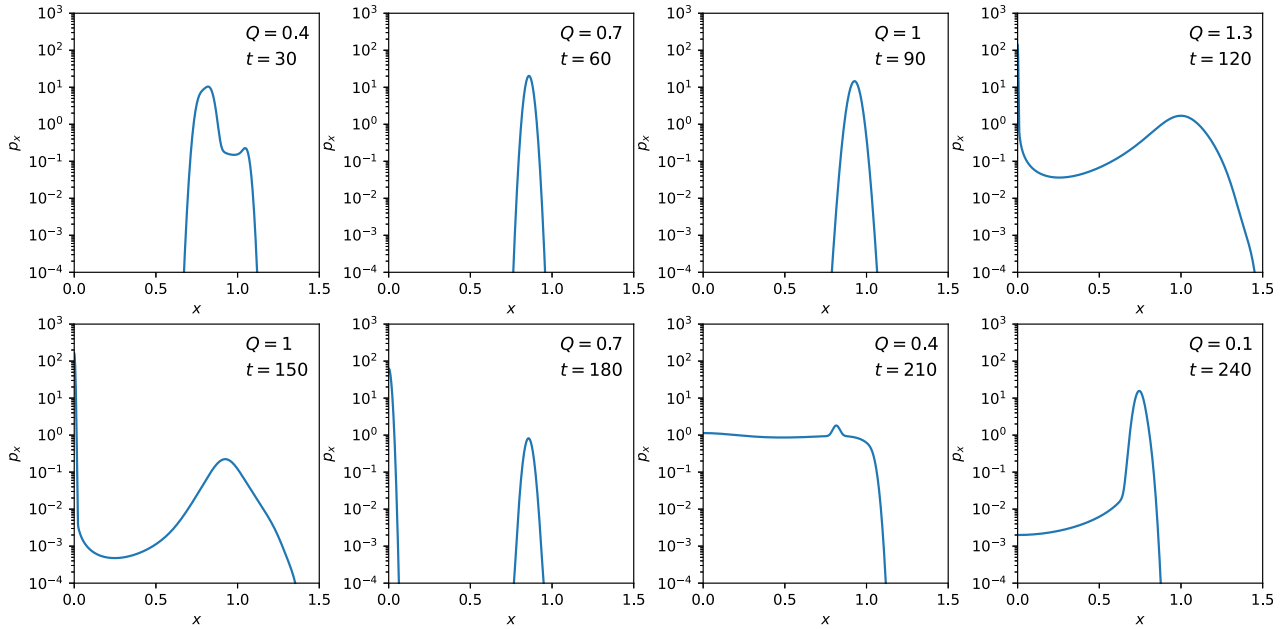
FIG. 6. The marginal PDF p_x for $D_x = D_v = 10^{-4}$ for set 2.
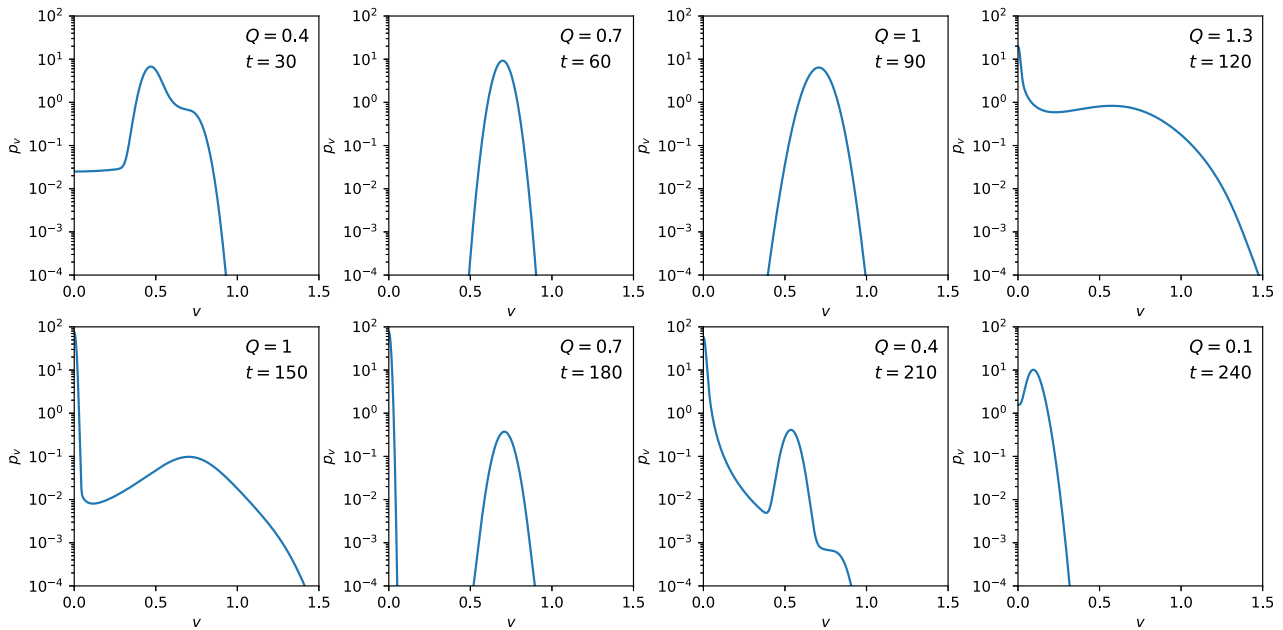

FIG. 7. The marginal PDF p_v for $D_x = D_v = 10^{-4}$ for set 2.

the mean flows become more dominant than in set 1. The implication is that the zonal flows are more significant when the power ramping is faster (set 1), suggesting non-equilibrium generation of zonal flows, and the mean flows are more significant when the power ramping is slower (set 2).

The Appendix shows stationary PDFs when a variety of constant powers are used, the powers being $Q = 0.8, 0.85, 0.9, 0.95, 1$. For the stationary PDFs, as the (constant) power increases the peak at the origin becomes stronger and the peak at finite (x, v) becomes weaker, as previously discussed the peak separation is greater for set 2 than set 1. In this
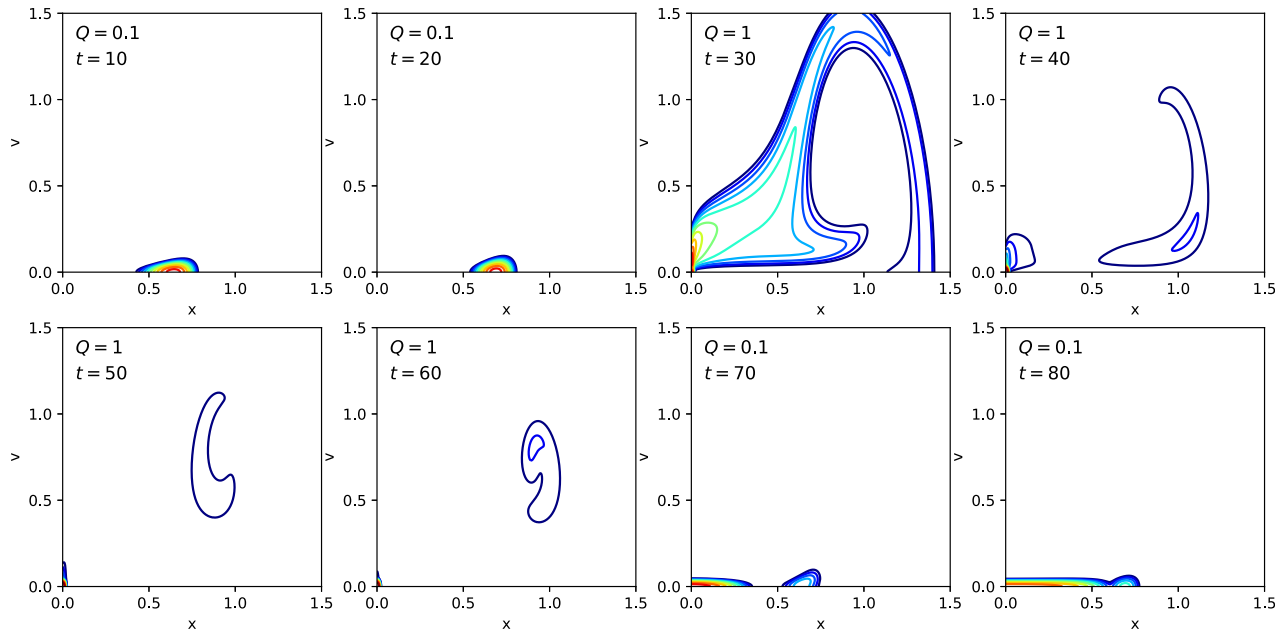
FIG. 8. Contour plots of the joint PDF $p(x, v, t)$ for $D_x = D_v = 10^{-4}$ in the (x, v) plane for set 3. The plots are labeled with the instantaneous time (t) and power (Q). The contours are on a logarithmic scale, ranging from 10^{-2} to 10^3 with intervals of $10^{0.5}$.

way, the PDFs for set 2 have closer proximity to the stationary PDFs, and vice versa for set 1. That is, set 1 evolves further from equilibrium.

2. Step Q

For set 3, the formation of a peak at the origin occurs closer in time to the turbulence-zonal flow dithering than in any other set, as

can be seen in Fig. 8 at time $t = 30$. There is limited time for turbulence-zonal flow self-regulation before the mean flow becomes dominant. The marginal PDFs p_x and p_v can be seen in Figs. 9 and 10, respectively. In Fig. 10 at $t = 30$, the long right tail of p_v around the global maximum can be seen, once again suggesting the role of intermittent zonal flows in the dithering. The origin peak is many orders of magnitude larger than the peak at finite (x, v). When the origin peak is
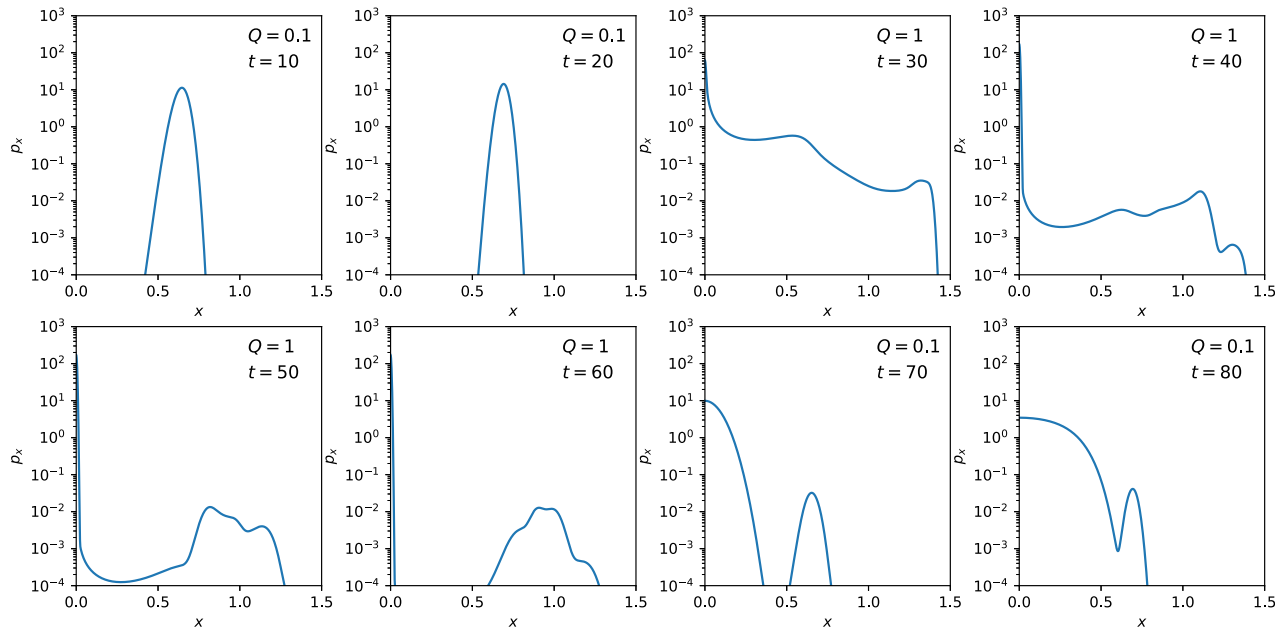

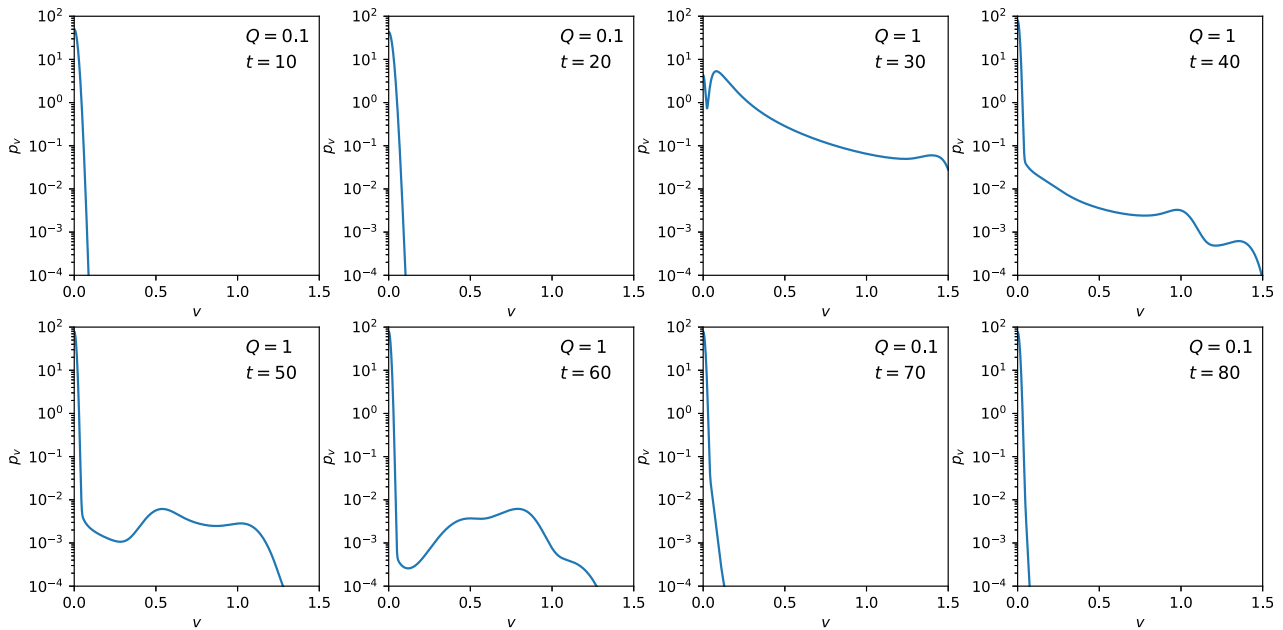**FIG. 9.** The marginal PDF p_x for $D_x = D_v = 10^{-4}$ for set 3.

FIG. 10. The marginal PDF p_v for $D_x = D_v = 10^{-4}$ for set 3.

maximum at $t = 60$, the peak at finite (x, v) is $\sim 0.0007\%$ its value for the joint PDF.

The joint PDF for set 4, shown in Fig. 11, shows dithering brought on by the power increase at $t = 10$, which is followed by the formation of a peak at the origin after the power increase at $t = 20$. The coexistence of dithering and origin peak formation can be seen at

$t = 30$. The bi-modality of the PDF is stronger for set 4 than set 3, when the peak at the origin is maximum at $t = 60$, the peak at finite (x, v) is $\sim 0.5\%$ its value. The power ramping in set 4 has resulted in the mean flow being less dominant than in set 3, and dithering solutions with finite (x, v) being more likely. The marginal PDFs p_x and p_v can be seen in Figs. 12 and 13, respectively. The form of p_v in Fig. 13 at
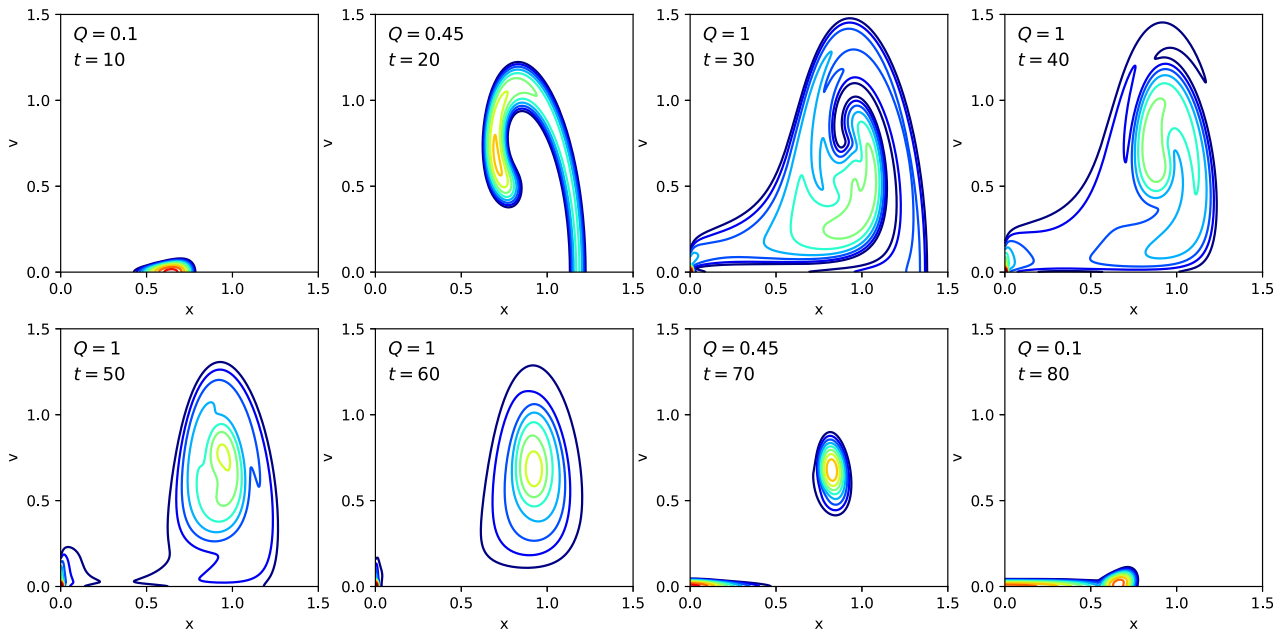

FIG. 11. Contour plots of the joint PDF $p(x, v, t)$ for $D_x = D_v = 10^{-4}$ in the (x, v) plane for set 4. The plots are labeled with the instantaneous time (t) and power (Q). The contours are on a logarithmic scale, ranging from 10^{-2} to 10^3 with intervals of $10^{0.5}$.
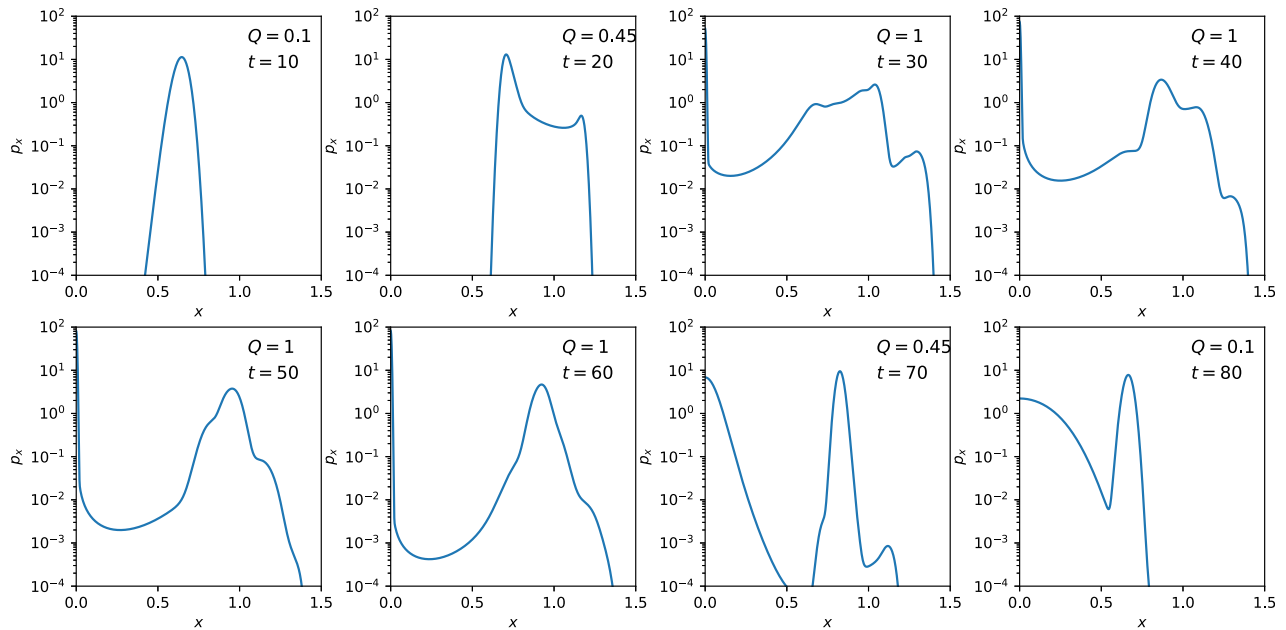
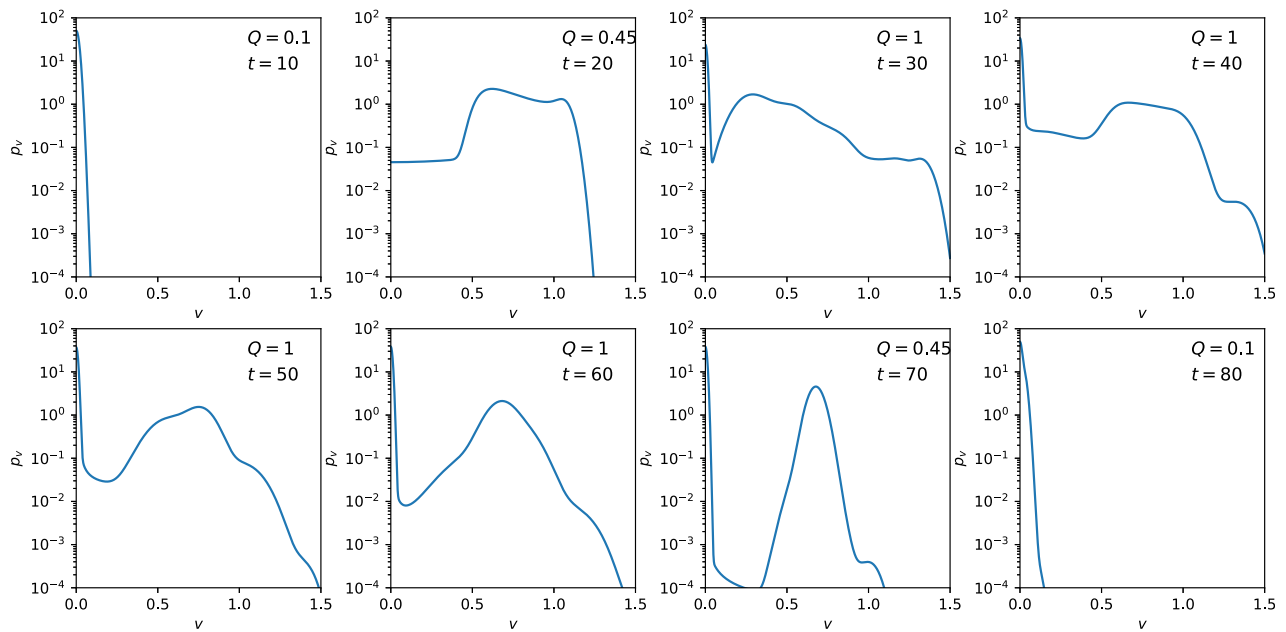**FIG. 12.** The marginal PDF p_x for $D_x = D_v = 10^{-4}$ for set 4.

FIG. 13. The marginal PDF p_v for $D_x = D_v = 10^{-4}$ for set 4.

$t = 20$ is reminiscent of set 1 with an even shallower tail between $v \sim 0.6$ and $v \sim 1.1$.

For set 5 in Fig. 14, we see dithering is the dominant behavior, and the formation of a peak at the origin which is never dominant, the opposite result to sets 3 and 4. At $t = 40$ and 50, the origin peak is $\sim 3\%$ of the peak at finite (x, v) in the joint PDF. The marginal PDFs

p_x and p_v are shown in Figs. 15 and 16, respectively. In p_v, shown in Fig. 16, we do not see a long tail toward large values of zonal flows, they have less contribution to the dithering.

Sets 3–5 demonstrate that the peak at the origin becomes weaker and the peak at finite (x, v) values becomes stronger with increasing the number of steps in Q prior to reaching $Q_{\max} = 1$, that is, the
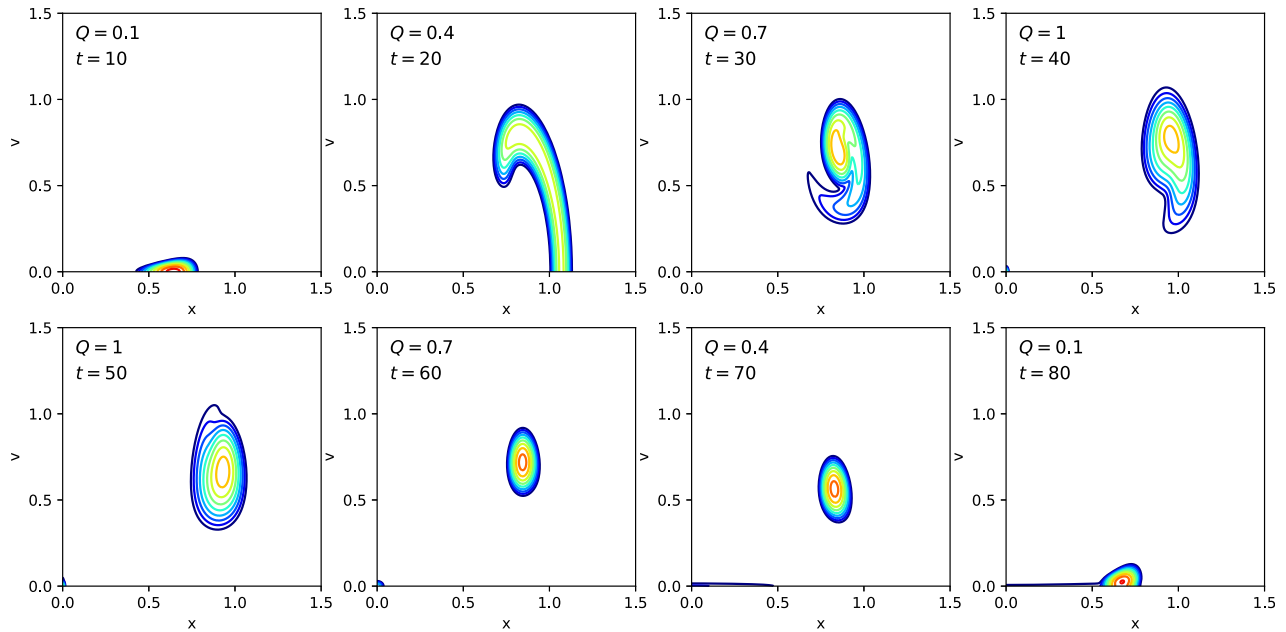
FIG. 14. Contour plots of the joint PDF $p(x, v, t)$ for $D_x = D_v = 10^{-4}$ in the (x, v) plane for set 5. The plots are labeled with the instantaneous time (t) and power (Q). The contours are on a logarithmic scale, ranging from 10^{-2} to 10^3 with intervals of $10^{0.5}$.
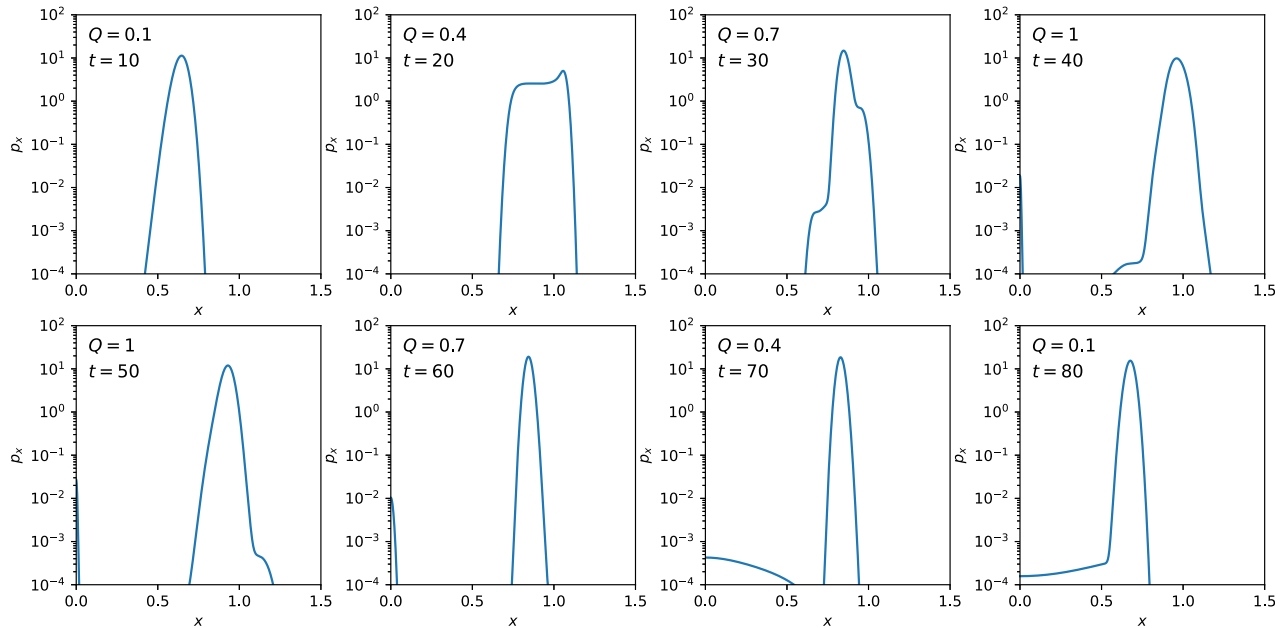
FIG. 15. The marginal PDF p_x for $D_x = D_v = 10^{-4}$ for set 5.

relative probability of H-mode states decreases, and the probability of dithering state increases. For set 3 there is a rapid development of a peak at the origin with little dithering, whereas for sets 4–5 the dithering is more prominent, occurring before and during the formation of a

peak at the origin. H-mode is more dominant in set 3 than set 4 despite Q_{max} being held for the same amount of time, the intermediate step in power for set 4 leading to more dithering. The reduced probability of H-mode for set 5 compared to sets 3,4 is probably due to Q_{max}

FIG. 16. The marginal PDF p_v for $D_x = D_v = 10^{-4}$ for set 5.

being held for half the time, despite the total energy input being equal for sets 3 and 5.
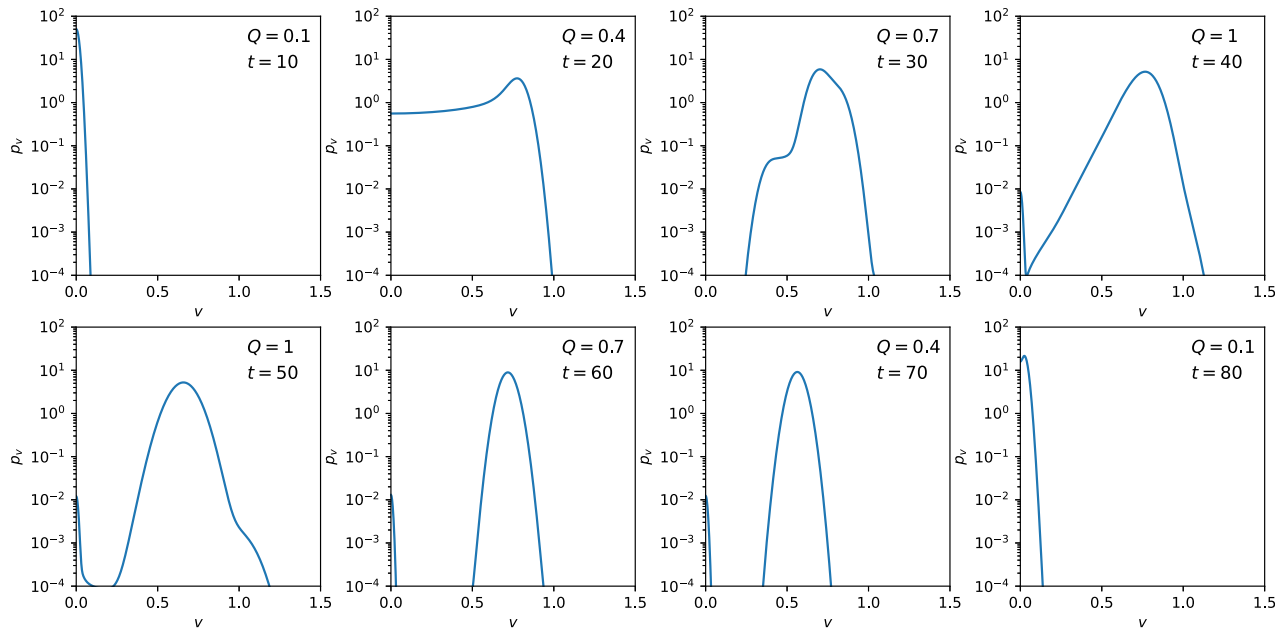
The relevance of intermittent zonal flows to the dithering dynamics has been discussed for all sets. What we can see in the structure of p_v across the sets is a longer tail toward larger zonal flows when the power has a faster ramping rate (for the linear cases) and when the power is more discontinuous (larger steps) for the step rampings.

B. Mean, standard deviation, cross correlation and phase portrait

The means $\langle x \rangle$ and $\langle v \rangle$, standard deviations σ_x and σ_v, and cross correlation σ_{xv} are calculated from the joint PDF and are discussed here. The results for set 1 are shown in Fig. 17. In the forward process, we can see the rapid growth of $\langle v \rangle$ starting at $t \sim 10$ due to the turbulence-zonal flow interaction, followed by an oscillatory phase in $\langle x \rangle$ and $\langle v \rangle$, which shows the turbulence-zonal flow self-regulation, both $\langle x \rangle$ and $\langle v \rangle$ oscillate from $t \sim 15$ to $t \sim 60$. As we saw in Fig. 2, the formation of second peak at the origin from $t = 40$ onward renders the means of little use to understand the dynamics. From $t \sim 40$ onward, $\langle x \rangle$ and $\langle v \rangle$ show a mixture of the H-mode and dithering states. The standard deviations, which are shown in column 2 of Fig. 17, also show oscillation, starting at $t \sim 15$. During the forward process σ_v is larger than σ_x, the ordering reverses at $t \sim 40$ and for the backward process σ_x is the larger of the two. The sudden increases in σ_x, σ_v at $t \sim 10$ and $t \sim 35$ correspond to the transitions to dithering and H-mode, respectively, where there is an increase in fluctuations. The cross correlation σ_{xv}, shown in column 3, shows greater variation in the forward process than the backward process. The phase portrait in column 4 shows the attractor type structure which $\langle x \rangle$ and $\langle v \rangle$ move around.

The results for set 2 are shown in Fig. 18. The initial increase in $\langle x \rangle$ and then $\langle v \rangle$ is similar to that in Fig. 17, after which there is

oscillation with a reduced amplitude compared to set 1. It was noted the PDF for set 2 shows weaker bi-modality compared to set 1, so the means provide a better representation of the dynamics. The rapid decrease in $\langle x \rangle$ and $\langle v \rangle$, starting just before Q_{max} is reached, reflects the greater dominance of H-mode for this set. The standard deviations are shown in column 2, both σ_x and σ_v have three stages where there is a rapid increase; these correspond to transitions to dithering, H-mode and L-mode. This can be seen in the PDF in Fig. 5. For the majority of the forward process, σ_v is larger than σ_x whereas for the majority of the backward process σ_x is larger than σ_v, σ_x overtaking σ_v during the formation of the peak at the origin. The cross correlation in column 3 shows greater variation in the forward process than the backward process. In the forward process σ_{xv} is similar for sets 1 and 2, the key difference being more oscillation for set 1.

The final comparison is between sets 3–5. These are shown in Fig. 19. For set 3, the rapid increase in $\langle v \rangle$ shortly after the power increase at $t = 20$ shows the turbulence-zonal flow interaction, before both $\langle x \rangle$ and $\langle v \rangle$ rapidly decrease due to the formation of a strong peak at the origin in the PDF. For set 4, $\langle x \rangle$ and $\langle v \rangle$ capture the turbulence-zonal flow dithering but the stronger bi-modality seen in the PDF for set 4 compared to set 3 means $\langle x \rangle$ and $\langle v \rangle$ contain a mixture of H-mode and dithering states. The largest changes in σ_x, σ_v again occur for the transitions to dithering, H-mode and L-mode, the prolonged oscillation between $t = 30$ and $t = 60$ reflects the power being held constant during this time. For set 5, $\langle x \rangle$ and $\langle v \rangle$ have a similar evolution to those in set 4 except they oscillate around larger values of x and v due to the (weaker) stronger peak at (the origin) finite x, v in the PDF. The large increases in σ_x and σ_v at $t \sim 20$ are similar to those seen in set 4 as in both sets they correspond to the transition to dithering. There is no further large increases in σ_x and σ_v since there is no transition to H-mode.

FIG. 17. Mean, standard deviation and cross correlation for set 1. Column 1 shows $\langle x \rangle$ and $\langle v \rangle$ as functions of time, with $\langle x \rangle$ in blue and $\langle v \rangle$ in red. Column 2 shows the associated standard deviations σ_x and σ_v, with the same color-coding. Column 3 shows the cross correlation $\sigma_{xv} = \langle (x - \langle x \rangle)(v - \langle v \rangle) \rangle / (\sigma_x \sigma_v)$. Column 4 shows the phase portrait in the $(\langle x \rangle, \langle v \rangle)$ plane.
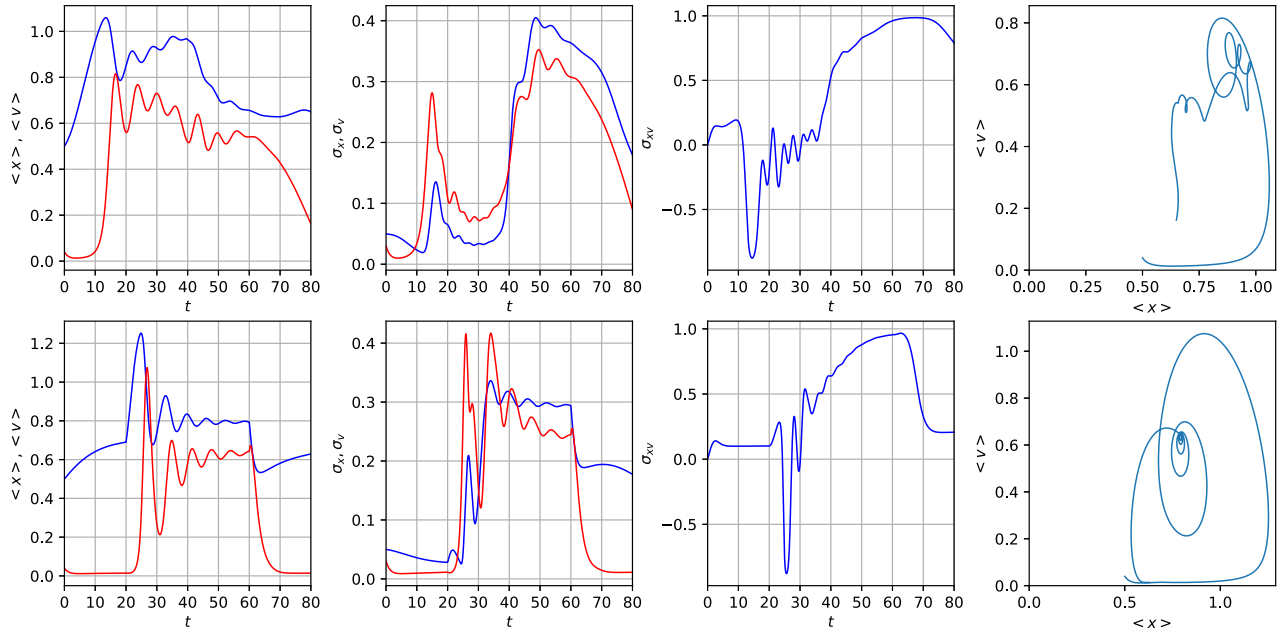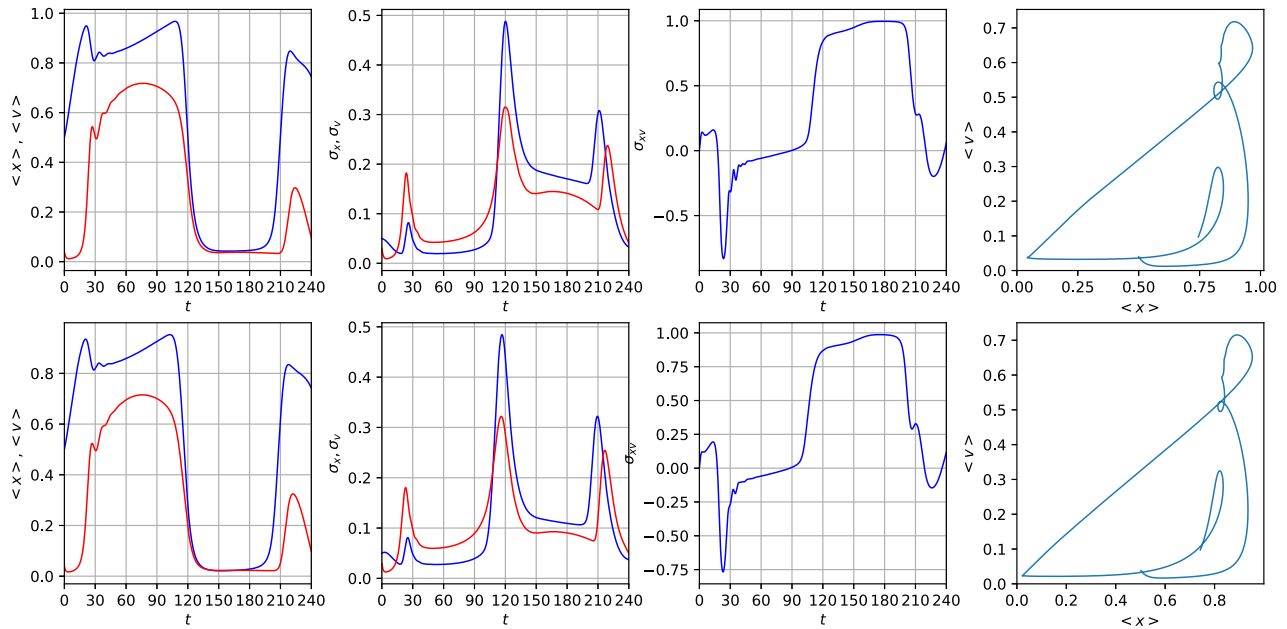

FIG. 18. Mean, standard deviation and cross correlation for set 2. Column 1 shows $\langle x \rangle$ and $\langle v \rangle$ as functions of time, with $\langle x \rangle$ in blue and $\langle v \rangle$ in red. Column 2 shows the associated standard deviations σ_x and σ_v, with the same colour-coding. Column 3 shows the cross correlation $\sigma_{xv} = \langle (x - \langle x \rangle)(v - \langle v \rangle) \rangle / (\sigma_x \sigma_v)$. Column 4 shows the phase portrait in the $(\langle x \rangle, \langle v \rangle)$ plane.

FIG. 19. Mean, standard deviation and cross correlation for set 3 (top row), set 4 (middle row), and set 5 (bottom row). Column 1 shows $\langle x \rangle$ and $\langle v \rangle$ as functions of time, with $\langle x \rangle$ in blue and $\langle v \rangle$ in red. Column 2 shows the associated standard deviations σ_x and σ_v, with the same color-coding. Column 3 shows the cross correlation $\sigma_{xv} = \langle (x - \langle x \rangle)(v - \langle v \rangle) \rangle / (\sigma_x \sigma_v)$. Column 4 shows the phase portrait in the $(\langle x \rangle, \langle v \rangle)$ plane.
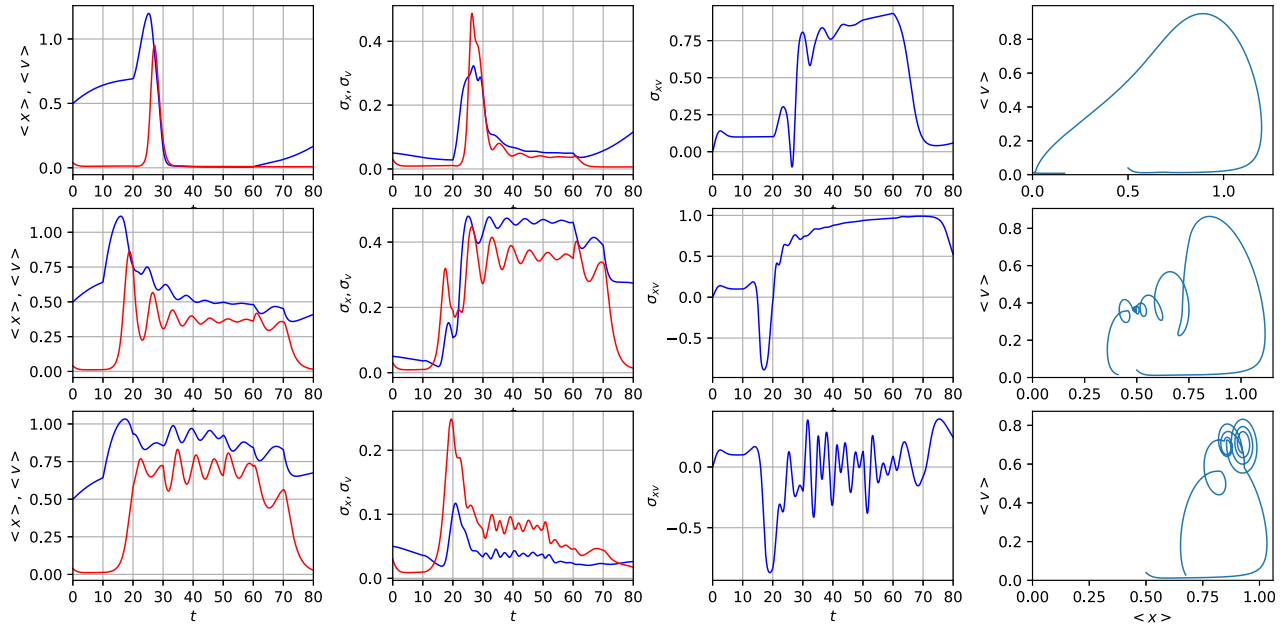
C. Information rate and length

Now the information rate and length diagnostics will be considered. The information rate and length for set 1 is shown in Fig. 20, set 2 is shown in Fig. 21, and sets 3–5 are shown in Fig. 22.

1. Information rate

Starting with set 1, for the majority of the simulation time between $t \sim 15$ and $t \sim 60$, Γ_x and Γ_v oscillate around $\Gamma_x = \Gamma_v$. The oscillation shows the rate of change of the marginal PDFs are
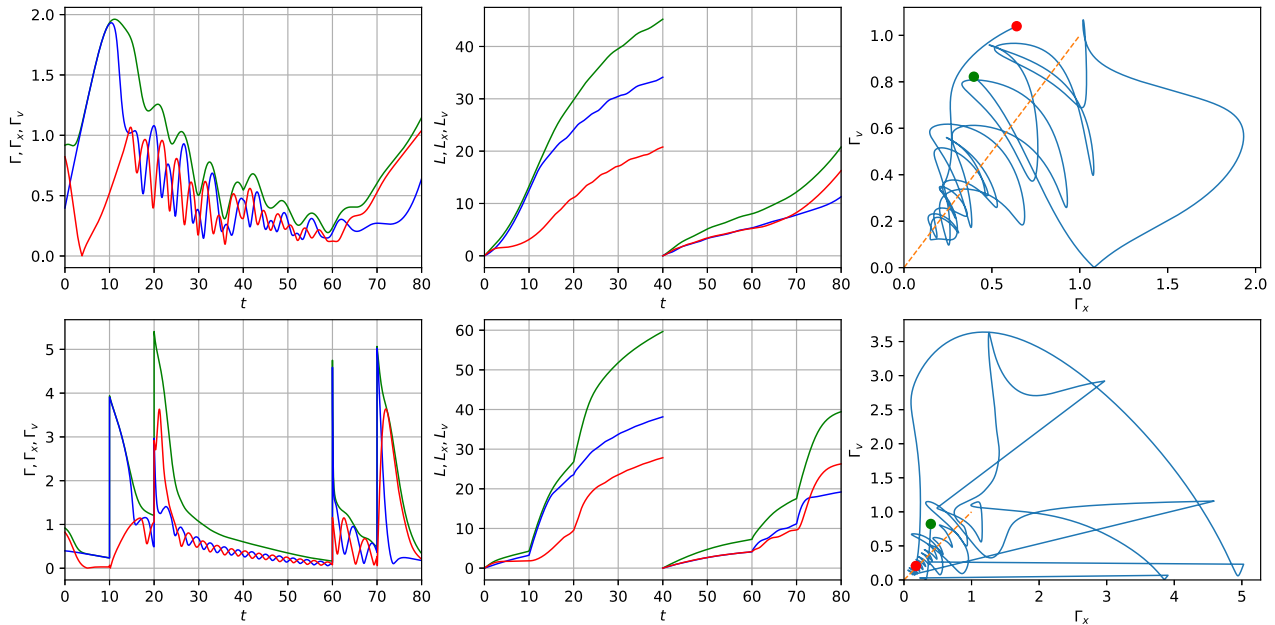
FIG. 20. The information geometry diagnostics for set 1. Column 1 shows Γ (green), Γ_x (blue), and Γ_v (red) as functions of time. Column 2 shows $\mathcal{L}$ (green), $\mathcal{L}_x$ (blue), and $\mathcal{E}_v$ (red) as functions of time. Column 3 shows the phase portrait in the (Γ_x, Γ_v) plane; $t = 0$ is shown by the green dot and $t = 80$ by the red dot; the dashed line shows $\Gamma_x = \Gamma_v$.

FIG. 21. The information geometry diagnostics for set 2. Column 1 shows Γ (green), Γ_x (blue), and Γ_v (red) as functions of time. Column 2 shows $\mathcal{L}$ (green), $\mathcal{L}_x$ (blue), and $\mathcal{E}_v$ (red) as functions of time. Column 3 shows the phase portrait in the (Γ_x, Γ_v) plane; $t = 0$ is shown by the green dot and $t = 80$ by the red dot; the dashed line shows $\Gamma_x = \Gamma_v$.
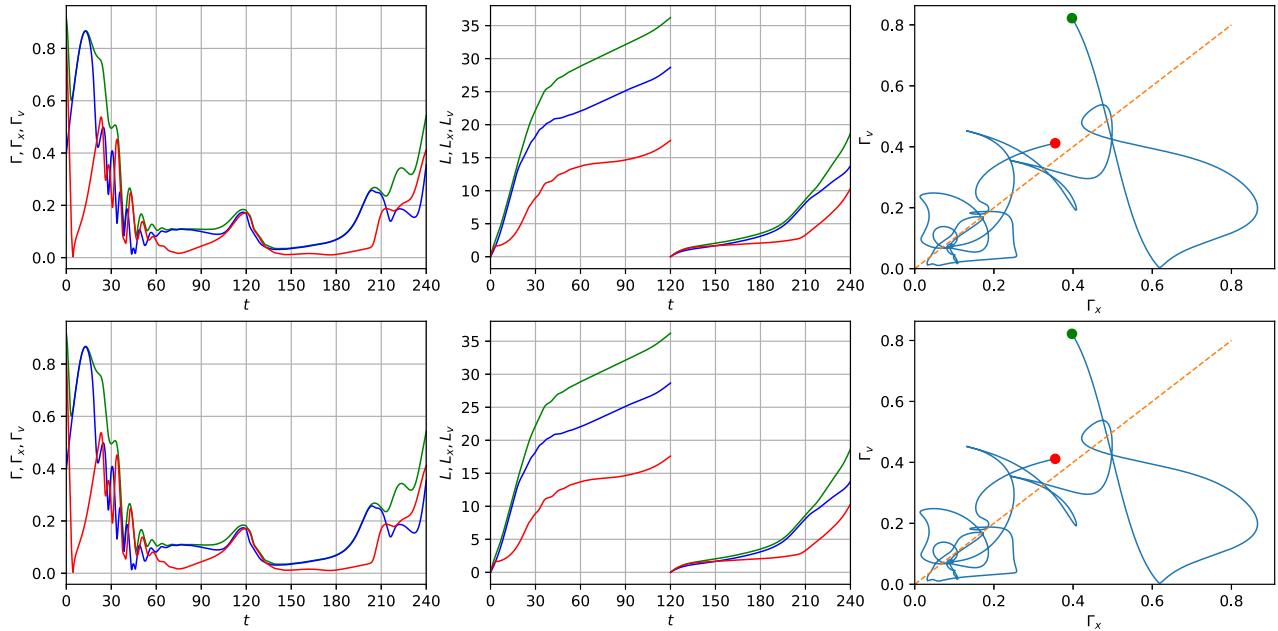
matching along the path, but with a phase shift. This can be seen in the phase portrait in the rightmost column of Fig. 20 where there are many crossings of the $\Gamma_x = \Gamma_v$ line. This relationship between Γ_x and Γ_v implies self-regulation between

turbulence and zonal flows in terms of the evolution of their statistical states.

For set 2, there is also evidence of self-regulation between turbulence and zonal flows: Γ_x and Γ_v oscillate around $\Gamma_x = \Gamma_v$ between
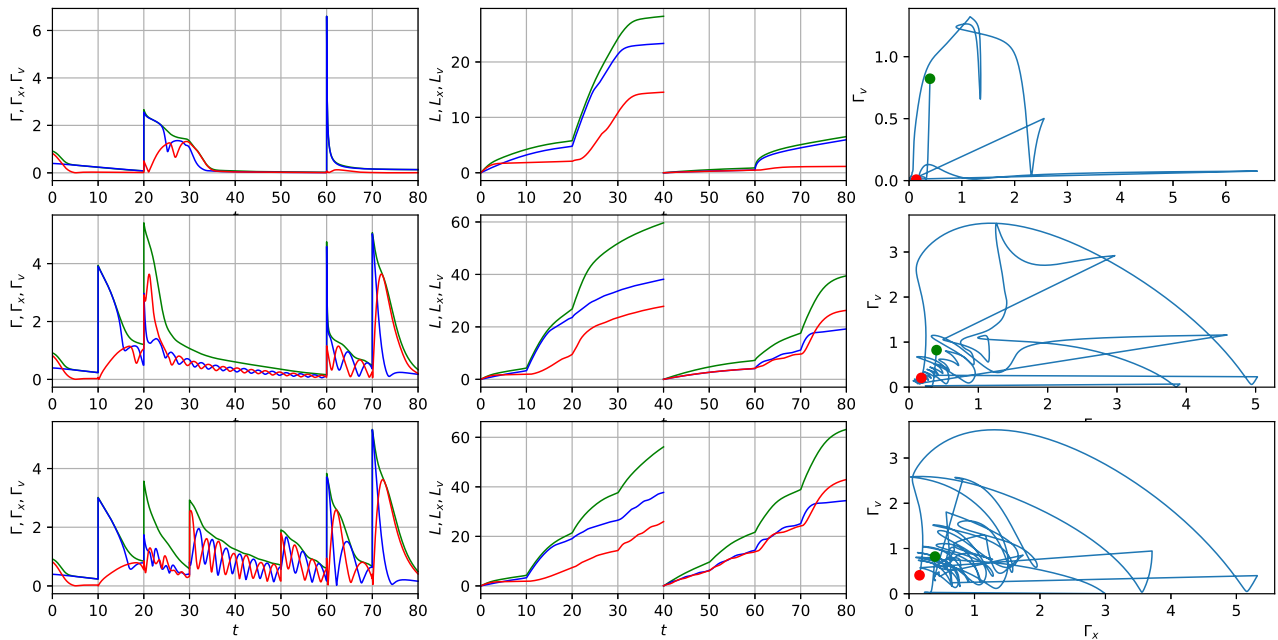
FIG. 22. The information geometry diagnostics for set 3 (top row), set 4 (middle row) and set 5 (bottom row). Column 1 shows Γ (green), Γ_x (blue), and Γ_v (red) as functions of time. Column 2 shows $\mathcal{L}$ (green), $\mathcal{L}_x$ (blue), and $\mathcal{E}_v$ (red) as functions of time. Column 3 shows the phase portrait in the (Γ_x, Γ_v) plane. The starting point is shown by a green dot and the end point by a red dot.

$t \sim 20$ and $t \sim 60$. Comparing the results to those from set 1: the duration of oscillation is shorter for set 2; the values of Γ, Γ_x and Γ_v are consistently smaller for set 2. The reduced information rate reflects the slower changing input power. The oscillations of Γ_x and Γ_v are much more pronounced than those of $\langle x \rangle$ and $\langle v \rangle$, this is for the initial oscillation starting at $t \sim 20$. The increased sensitivity of the information rate to dithering compared to the means is also seen at $t \sim 200$ where there is oscillation of Γ and Γ_x but no oscillation of $\langle x \rangle$.

Sets 3–5 are characterized by (large) spikes in Γ and Γ_x when there is a change in power, and significantly smaller spikes in Γ_v; Γ_v tends to increase more gradually after the power change as zonal flows need time to react. The larger response from Γ_x (and Γ) at the power steps is because in our model the coupling between the input power and turbulence is stronger than the coupling between the input power and zonal flow. This can be seen in the model equations where (due to the density gradient approximation) the input power appears in growth and damping terms for x [Eq. (5)], whereas the input power only appears as a damping term for the zonal flow [Eq. (6)]. The power decrease in set 3 at $t = 60$ results in the largest value of Γ and Γ_x seen across all the power rampings. For sets 4 and 5, there is significant oscillation of Γ_x and Γ_v around $\Gamma_x = \Gamma_v$, whereas for set 3, there is virtually no evidence of self-regulation. It can be seen for sets 4 and 5 the amplitude of oscillation for Γ_x, Γ_v is significantly larger than Γ; for the cases of a linearly increasing input power the amplitude of oscillation is similar for Γ, Γ_x and Γ_v. The spikes in the information rate give a clear indication of the sudden change to the system input, this is harder to discern from the means, standard deviations and cross correlation.

The information rate is larger when the power changes more abruptly, this can be seen for the faster linear ramping compared to the slower linear ramping and also for the step changes in power. This reflects the rapid evolution of a system in response to faster change in input power. The effect of a step change in power is an extremely rapid response from the information rate.

2. Information length

For each set, the information length has been reset to 0 at the midpoint so the information change in the forward and backward processes can be compared. The final information lengths for the forward and backward processes are given in Table I.

For set 1, the total information change is greater in the forward process than in the backward process, as can be seen in the larger values of $\mathcal{L}$, $\mathcal{L}_x$, and $\mathcal{L}_v$ at $t = 40$ compared to $t = 80$ in Fig. 20. In the

forward process, $\mathcal{L}_x$ is nearly always larger than $\mathcal{L}_v$, however in the backward process $\mathcal{L}_x \sim \mathcal{L}_v$ between $t = 40$ and $t = 70$. The final values of $\mathcal{L}_v$ (at the end of the forward and backward processes) are more similar than the corresponding values of $\mathcal{L}_x$, suggesting greater sensitivity in the turbulence to the power increase and decrease.

The information length for set 2 can be seen in the second column of Fig. 21. In both the forward and backward processes, the total information lengths ($\mathcal{L}$, $\mathcal{L}_x$, and $\mathcal{L}_v$) are smaller for set 2 than set 1, meaning the total information change is less for the slower ramping. For set 2, like set 1, the total information change is greater in the forward process than the backward process. The difference between the final information length for the forward and backward processes ($\Delta \mathcal{L}$) is reduced for set 2, showing the slower ramping is able to maintain the system closer to equilibrium.

For the stepwise power increase in sets 3–5, increasing the number of steps produces a more symmetric information length between the forward and backward processes, as seen in the second column of Fig. 22. It can be seen in Table I the relative $\Delta \mathcal{L}$ decreases as the number of steps increase. The reduced hysteresis by increasing the number of steps shows the PDF is able to remain closer to equilibrium.

D. Entropy

First, it is worth noting for all sets the entropy flux to the environment is not plotted as it cannot be distinguished from the total entropy production rate; the relative deviation of the entropy production from the entropy flux is extremely small. For the input powers investigated here there is a consistent flow of entropy from the system to the environment.

The entropy diagnostics for set 1 can be seen in Fig. 23. In the forward process, the rate of entropy production, $\dot{S}_T$, is dominated by the entropy production in v. In the backward process, the contribution to the rate of entropy production from x and v is more even.

The rate of entropy production is largest at $t \sim 15$; around the time, we see the onset of dithering across the diagnostics. There is dithering in $\dot{S}_T$, which is more pronounced than the dithering in S. (S also has a peak at $t \sim 15$ but it is not the global maximum.) Despite this, the entropy production during the backward process is larger than the forward process, the reverse of the information length (calculated from the joint PDF).

The entropy diagnostics for set 2 are shown in Fig. 24. Compared to set 1, the contribution of $\dot{S}_{Tx}$ and $\dot{S}_{Tv}$ to $\dot{S}_T$ is more even, the profile of both the components is similar in how they have three peaks at approximately the same times. The rate of entropy production peaks

TABLE I. Summary table of time-integrated quantities at the end of the forward and backward processes for each of the sets. Also shown is the maximum power (Q_{max}) and the total energy input (E_{in}) for each set.

| Set | Forward | | | | | | Backward | | | | | | | |
	$\mathcal{L}$	$\mathcal{L}_x$	$\mathcal{L}_v$	S_T	S_{Tx}	S_{Tv}	$\mathcal{L}$	$\mathcal{L}_x$	$\mathcal{L}_v$	S_T	S_{Tx}	S_{Tv}	Q_{max}	E_{in}
1	45.2	34.1	20.8	6900	1411	5488	20.8	11.3	16.3	7903	2326	5576	1.3	56
2	36.2	28.7	17.6	12 642	5497	7145	18.7	13.8	10.3	8808	5057	3751	1.3	168
3	28.2	23.3	14.5	21 092	5639	15 453	6.5	6.0	1.1	99	40	59	1.0	44
4	59.7	38.1	27.8	18 069	4049	14 020	39.4	19.2	26.3	4520	857	3663	1.0	56
5	56.1	37.7	26.0	5516	1043	4473	63.2	34.4	42.9	2908	537	2372	1.0	44

FIG. 23. Entropy diagnostics for set 1. Column 1 shows the total entropy production rate $\dot{S}_T$ (green), $\dot{S}_{Tx}$ (blue), and $\dot{S}_{Tv}$ (red). Column 2 shows the total entropy S_T (green), S_{Tx} (blue), and S_{Tv} (red); these have been set to zero at the beginning of the backward process. Column 3 shows the entropies S (green), S_x (blue), and S_v (red).
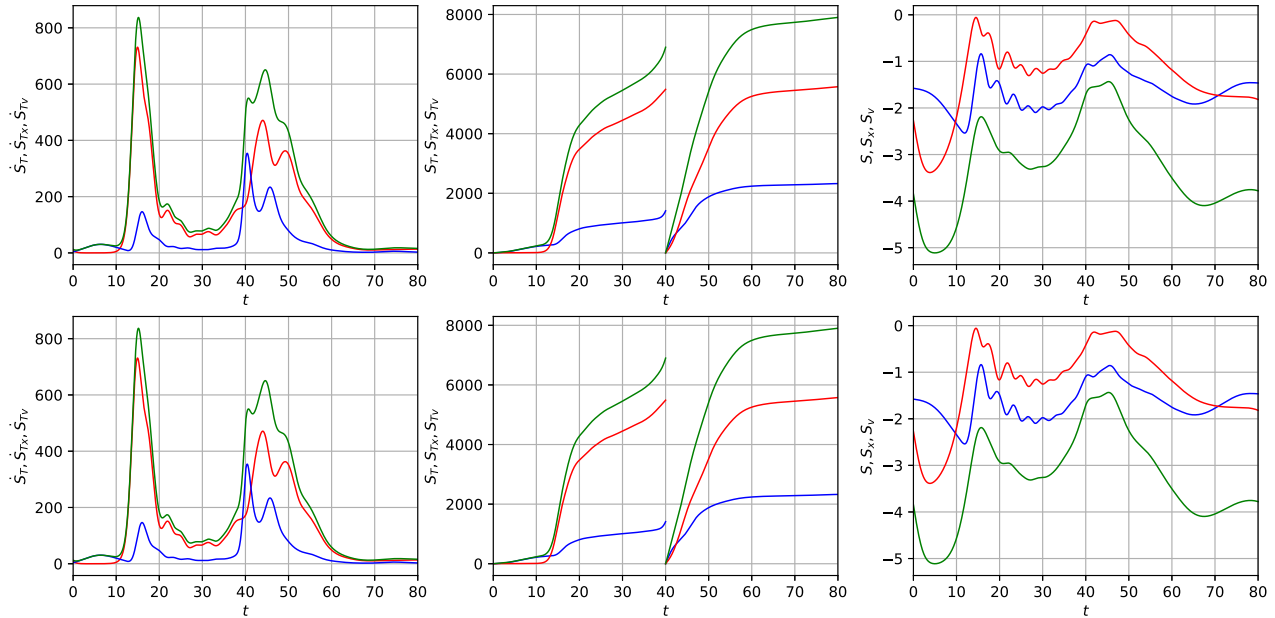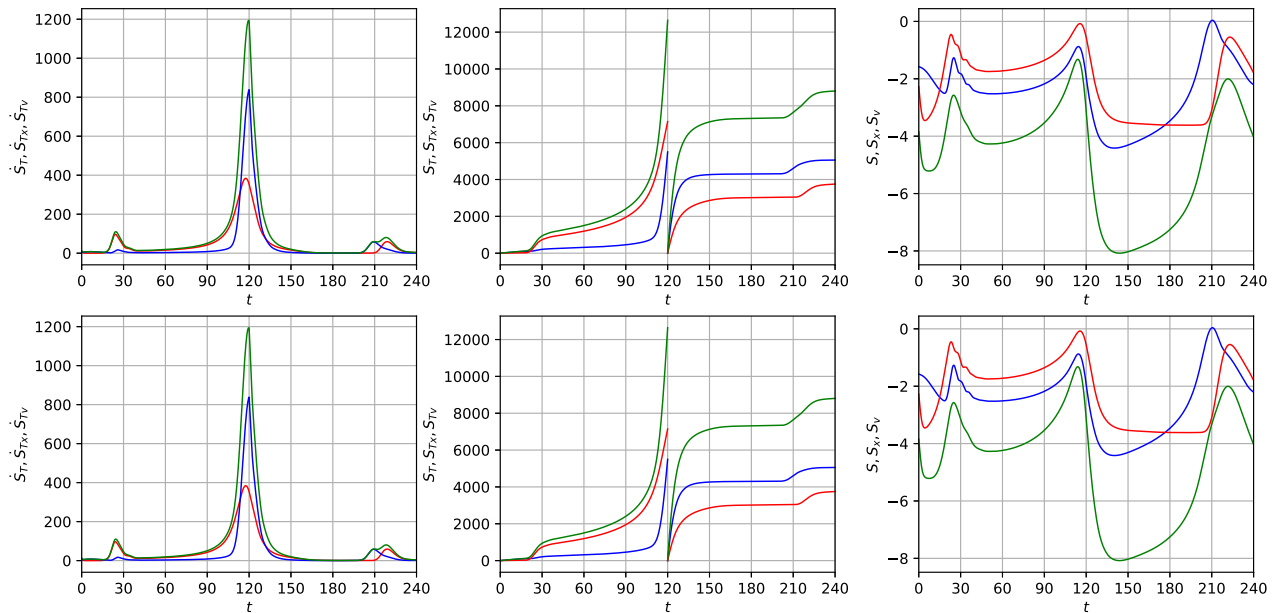

FIG. 24. Entropy diagnostics for set 2. Column 1 shows the total entropy production rate $\dot{S}_T$ (green), $\dot{S}_{Tx}$ (blue), and $\dot{S}_{Tv}$ (red). Column 2 shows the total entropy S_T (green), S_{Tx} (blue), and S_{Tv} (red); these have been set to zero at the beginning of the backward process. Column 3 shows the entropies S (green), S_x (blue), and S_v (red).

at $t \sim 120$; in Fig. 5, there is the formation of a strong peak at the origin between $t = 90$ and $t = 120$, during this interval S_T monotonically increases from ~ 50 to ~ 1200, showing the L–H transition is accompanied by a large increase in the total entropy production.

The largest increase in $\dot{S}_T$ for set 1 correspond to the transitions to dithering and H-mode, and for set 2 they correspond to transitions to dithering, H-mode and L-mode. The entropy S also has these structures, seen in column 3 of Figs. 23 and 24; however, the equivalent
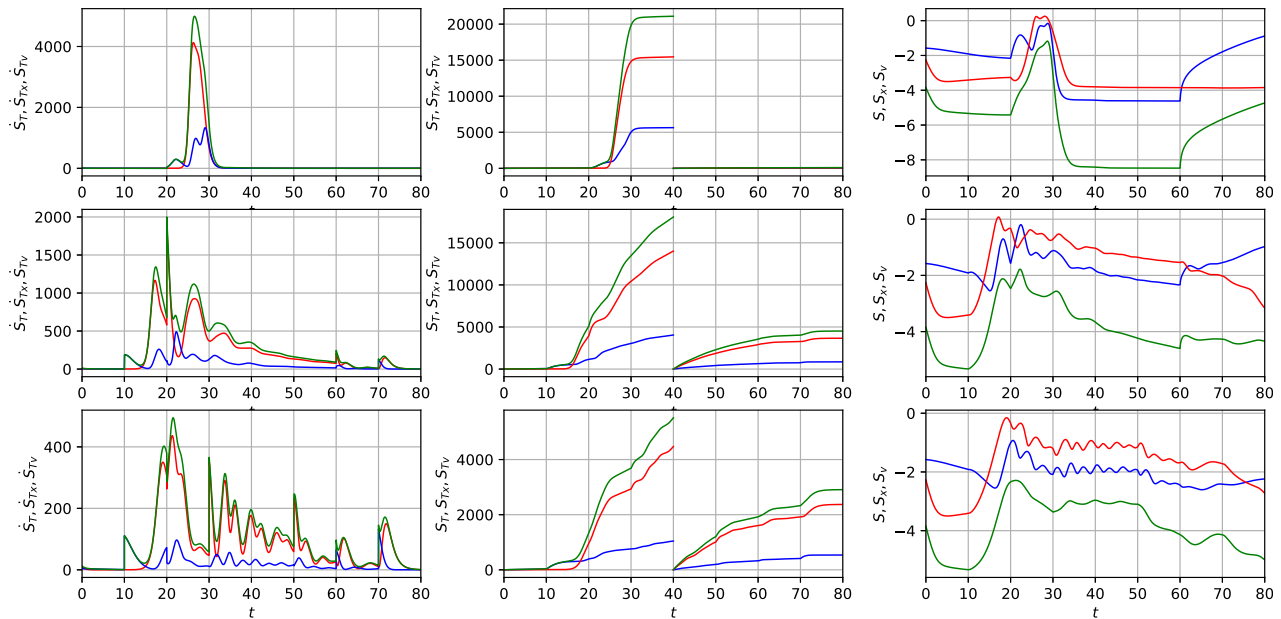
FIG. 25. Entropy diagnostics for set 3 (top row), set 4 (middle row), and set 5 (bottom row). Column 1 shows the total entropy production rate $\dot{S}_T$ (green), $\dot{S}_{Tx}$ (blue), and $\dot{S}_{Tv}$ (red). Column 2 shows the total entropy S_T (green), S_{Tx} (blue), and S_{Tv} (red); these have been set to zero at the beginning of the backward process. Column 3 shows the entropies S (green), S_x (blue), and S_v (red).

peaks have very similar values for sets 1 and 2. The values for the first peak are within 20% of each other, and the values of the second peak are within 10% of each other. The values of $\dot{S}_T$ have a larger relative difference and emphasize the difference in scale of dithering and (origin) peak formation that is seen in the PDFs. Greater entropy production is associated with the formation of a stronger peak at the origin, $\dot{S}_T$ for set 2 at $t \sim 120$ is approximately twice $\dot{S}_T$ for set 1 at $t \sim 45$. Greater entropy production is also associated with stronger turbulence-zonal flow dithering, $\dot{S}_T$ for set 1 at $t \sim 15$ is approximately eight times $\dot{S}_T$ for set 2 at $t \sim 20$.

There is a larger relative difference in the total entropy S_T at the end of the forward and backward processes for set 2 than set 1, the opposite result to the information length. Based on the observation made at the end of Linear Q about set 2 remaining closer to equilibrium, it could be said the information length provides a better measure of the proximity to equilibrium than the total entropy.

The entropy diagnostics for sets 3–5 are shown in Fig. 25. Similar to the information length, there is the tendency for the total entropy production to become more symmetric across the forward and backward processes as the number of steps increases. For the forward process, increasing the number of steps, and therefore decreasing the size of the steps, results in lower entropy production. For all sets, the rate of entropy production is dominated by $\dot{S}_{Tv}$, leading to greater entropy production in v than x in both the forward and backward processes. This is even true for set 3 where S_{Tx} and S_{Tv} are orders of magnitude less at the end of the backward process, see Table I. There are clear spikes in $\dot{S}_T$ when there is a step in power, which are also seen in Γ, however, all spikes in Γ have order of magnitude 10^0 (Γ is often larger when the power decreases) whereas for $\dot{S}_T$ the orders of magnitude span 10^0–10^3. After the spikes $\dot{S}_T$ is non-monotonic, whereas Γ tends

to monotonically decrease after the spikes. The spikes in Γ when there is a step in power are the largest values of Γ, after which there is a monotonic decrease; the spikes in $\dot{S}_T$ are often not the largest values as they are followed by significant increases, this can be seen most acutely for set 3 in the top row of Fig. 25. This shows a delay in the response of $\dot{S}_T$ compared to Γ.

VI. CONCLUSION

A stochastic, prey–predator model of the L–H transition in fusion plasma has been investigated. The model concerns the regulation of turbulence by zonal and mean flow shear. Independent delta-correlated Gaussian stochastic noises are used to construct Langevin equations for the amplitudes of turbulence and zonal flows. We then find numerical solutions of the equivalent Fokker–Planck equation for the time-dependent joint probability distribution of these quantities. We have extended the earlier studies presented in Refs. 22 and 23, by applying different functional forms of the time-dependent external heating (input power) which is increased and then decreased in a symmetric fashion to study hysteresis. The input powers are linear functions and step functions. The hysteresis is examined through the probability distribution and statistical measures, which include information geometry and entropy. The main findings of the work include (i) strongly non-Gaussian probability distributions with bi-modality being a persistent feature across the input powers; (ii) the information length to be a better indicator of distance to equilibrium than the total entropy; and (iii) dithering and the L-H transition are seen when the input power is stepped in time. By increasing the number of steps to reach the same $Q_{\max}$, we see less hysteresis (in the statistical measures) and a reduced probability of H-mode access; (iv) intermittent zonal flows are suggested to have a role in the initial suppression of

turbulence by zonal flows. This was observed in Ref. 23 and has now been observed for step power rampings; (v) stronger excitation of intermittent zonal flows for a faster changing input power, both for linear and step rampings; and (vi) the information rate and length continue to be useful to understand the correlation and self-regulation between the turbulence and zonal flows.

AUTHOR DECLARATIONS
Conflict of Interest

The authors have no conflicts to disclose.

Author Contributions

Patrick Fuller: Conceptualization (lead); Data curation (lead); Formal analysis (lead); Investigation (lead); Methodology (equal); Software (supporting); Writing – original draft (lead); Writing – review & editing (equal). **Eun-jin Kim:** Formal analysis (supporting); Supervision (lead); Writing – review & editing (equal). **Rainer Hollerbach:** Software (lead); Supervision (supporting); Writing – review & editing (equal). **Bogdan Hnat:** Formal analysis (supporting); Supervision (lead); Writing – review & editing (equal).

DATA AVAILABILITY

The data that support the findings of this study are available from the corresponding author upon reasonable request.

APPENDIX: COMPARISON OF CONSTANT POWER L–H TRANSITION IN DETERMINISTIC AND STOCHASTIC MODELS

For the 2-ODE deterministic model, experimenting with different constant powers show there is a range of powers which result in turbulence (ϵ) increase which in turn triggers the growth of zonal flow shear (v). The turbulence and zonal flow shear have a prey–predator interaction and as time increases have relatively stable non-zero values. Above a threshold power the mean flow shear is larger and prevents the growth of the turbulence and zonal flow shear, both of which approach zero as time increases. For the model constants given in V and for initial values $\epsilon = 0.25$, $v = 10^{-2}$, the threshold power was found to be $Q = 0.832$ (to three figures).

The nature of the threshold power for the same initial turbulence and zonal flow shear but when there is stochastic noise was investigated. Figure 26 shows the PDF bifurcation into L-mode and
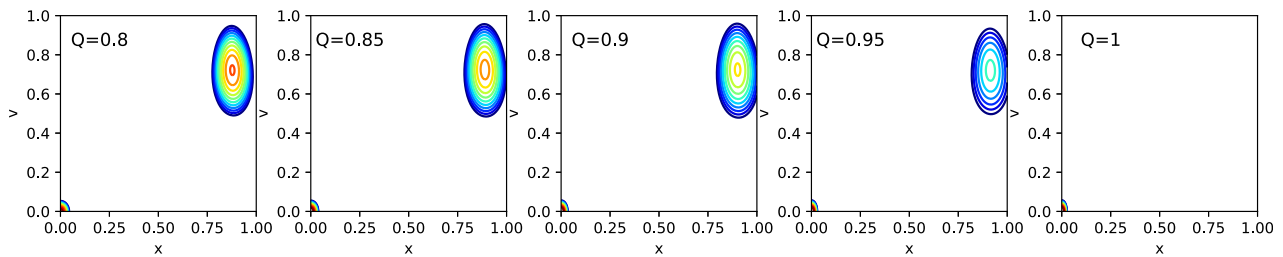
FIG. 26. Contour plots of the joint PDF $p(x, v, t)$ for $D_x = D_v = 10^{-4}$ in the (x, v) plane. The plots are labeled with the input power Q. All PDFs are taken at $t = 100$ when the PDF had become effectively stationary. The contours are on a logarithmic scale, ranging from 10^{-3} to 10^3 with intervals of $10^{0.5}$.
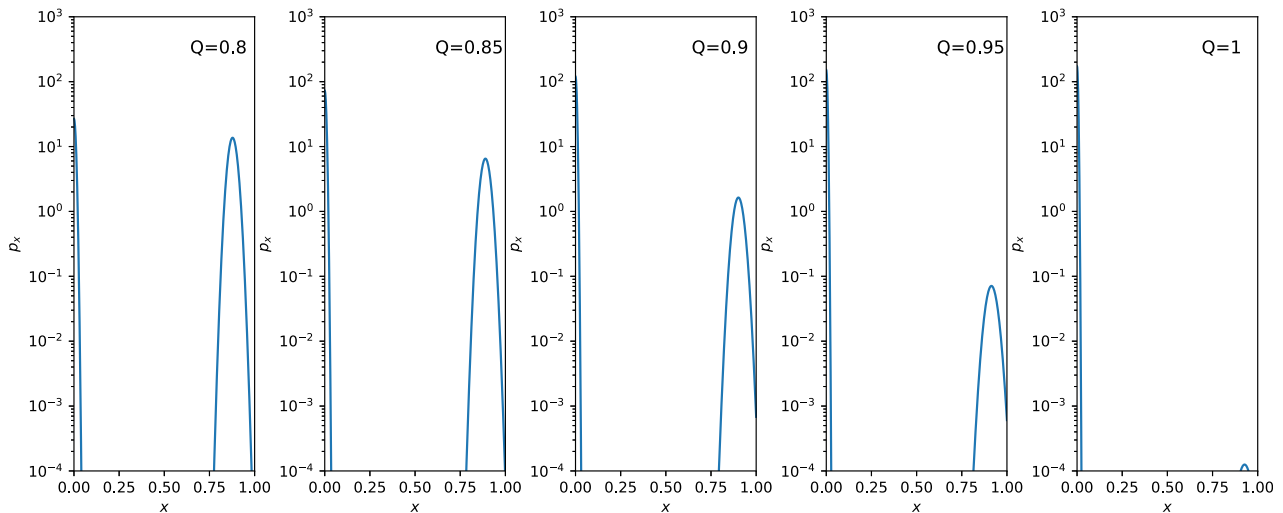

FIG. 27. The marginal PDF p_x for $D_x = D_v = 10^{-4}$. The plots are labeled with the input power Q. All PDFs are taken at $t = 100$ when the PDF had become effectively stationary.
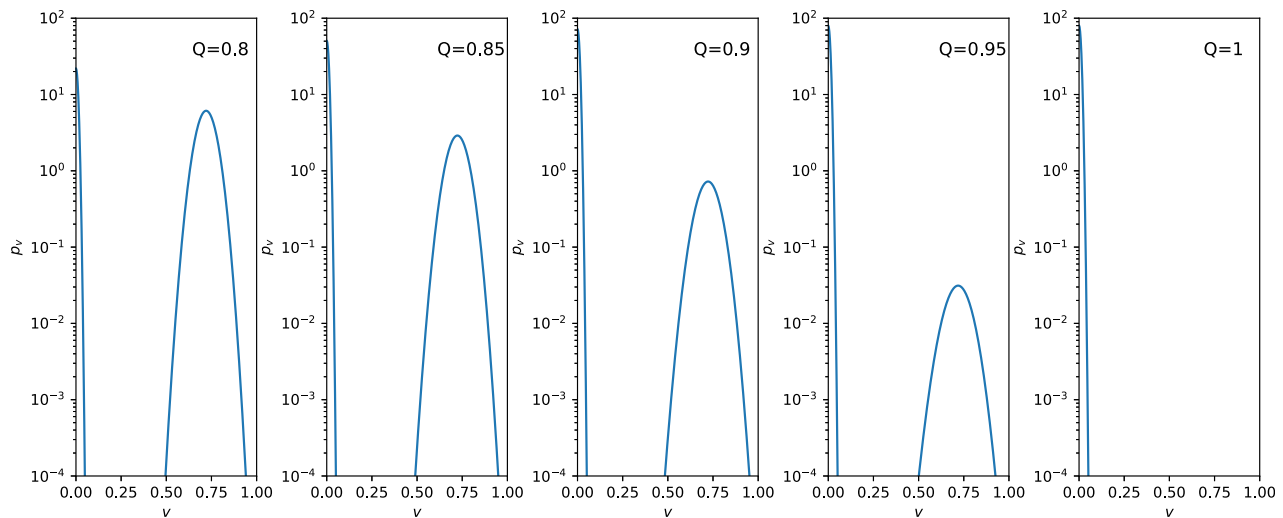
FIG. 28. The marginal PDF p_v for $D_x = D_v = 10^{-4}$. The plots are labeled with the input power Q. All PDFs are taken at $t = 100$ when the PDF had become effectively stationary.

H-mode states at $Q = 0.8$, meaning H-mode is possible at a lower power than in the deterministic model. The impact of the stochastic noise is to lower the power at which a quiescent H-mode is possible. It can also be seen in Fig. 26 that increasing the power causes the peak at the origin to increase and the peak at finite (x, v) to decrease. Increasing the power increases the proportion of solutions which access H-mode and decrease the proportion which access L-mode in the steady state. Therefore, in the stochastic model, there is not a sudden change above a threshold power like what occurs in the deterministic model, rather a gradual transition to the quiescent H-mode as the peak at the origin becomes larger. The marginal PDFs p_x and p_v for the various powers can be seen in Figs. 27 and 28.

REFERENCES

[1]F. Wagner, G. Becker, K. Behringer, D. Campbell, A. Eberhagen, W. Engelhardt, G. Fussmann, O. Gehre, J. Gernhardt, G. V. Gierke, G. Haas, M. Huang, F. Karger, M. Keilhacker, O. Klüber, M. Kornherr, K. Lackner, G. Lisitano, G. G. Lister, H. M. Mayer, D. Meisel, E. R. Müller, H. Murmann, H. Niedermeyer, W. Poschenrieder, H. Rapp, H. Röhr, F. Schneider, G. Siller, E. Speth, A. Stäbler, K. H. Steuer, G. Venus, O. Vollmer, and Z. Yü, "Regime of improved confinement and high beta in neutral beam-heated divertor discharges of the ASDEX tokamak," Phys. Rev. Lett. **49**, 1408–1412 (1982).

[2]L. Schmitz, L. Zeng, T. L. Rhodes, J. C. Hillesheim, E. J. Doyle, R. J. Groebner, W. A. Peebles, K. H. Burrell, and G. Wang, "Role of zonal flow predator-prey oscillations in triggering the transition to H-Mode confinement," Phys. Rev. Lett. **108**, 155002 (2012).

[3]L. Schmitz, L. Zeng, T. Rhodes, J. Hillesheim, W. Peebles, R. Groebner, K. Burrell, G. McKee, Z. Yan, G. Tynan, P. Diamond, J. Boedo, E. Doyle, B. Grierson, C. Chrystal, M. Austin, W. Solomon, and G. Wang, "The role of zonal flows and predator–prey oscillations in triggering the formation of edge and core transport barriers," Nucl. Fusion **54**, 073012 (2014).

[4]L. Schmitz, "The role of turbulence–flow interactions in L- to Hmode transition dynamics: Recent progress," Nucl. Fusion **57**, 025003 (2017).

[5]Y. R. Martin and T. Takizuka, and the ITPA CDBM H-mode Threshold Data Group. "Power requirement for accessing the H-mode in ITER," J. Phys.: Conf. Ser. **123**, 012033 (2008).

[6]E. Righi, D. Bartlett, J. Christiansen, G. Conway, J. Cordey, L.-G. Eriksson, H. D. Esch, G. Fishpool, C. Gowers, J. de Haas, P. Harbour, N. Hawkes, J. Jacquinot, T. Jones, W. Kerner, Q. King, C. Lowry, R. Monk, P. Nielsen, F. Rimini, G. Saibene, R. Sartori, B. Schunke, A. Sips, R. Smith, M. Stamp, D. Start, K. Thomsen, B. Tubbing, and N. Zornig, "Isotope scaling of the H mode power threshold on JET," Nucl. Fusion **39**, 309–319 (1999).

[7]H. Biglari, P. H. Diamond, and P. W. Terry, "Influence of sheared poloidal rotation on edge turbulence," Phys. Fluids B: Plasma Phys. **2**, 1–4 (1990).

[8]P. H. Diamond, Y.-M. Liang, B. A. Carreras, and P. W. Terry, "Self-regulating shear flow turbulence: A paradigm for the l to h transition," Phys. Rev. Lett. **72**, 2565–2568 (1994).

[9]S. J. Zweben, J. A. Boedo, O. Grulke, C. Hidalgo, B. LaBombard, R. J. Maqueda, P. Scarin, and J. L. Terry, "Edge turbulence measurements in toroidal fusion devices," Plasma Phys. Controlled Fusion **49**, S1 (2007).

[10]P. Beyer, S. Benkadda, X. Garbet, and P. H. Diamond, "Nondiffusive transport in tokamaks: Three-dimensional structure of bursts and the role of zonal flows," Phys. Rev. Lett. **85**, 4892–4895 (2000).

[11]J. F. Drake, P. N. Guzdar, and A. B. Hassam, "Streamer formation in plasma with a temperature gradient," Phys. Rev. Lett. **61**, 2205–2208 (1988).

[12]G. Y. Antar, S. I. Krasheninnikov, P. Devynck, R. P. Doerner, E. M. Hollmann, J. A. Boedo, S. C. Luckhardt, and R. W. Conn, "Experimental evidence of intermittent convection in the edge of magnetic confinement devices," Phys. Rev. Lett. **87**, 065001 (2001).

[13]B. A. Carreras, C. Hidalgo, E. Sánchez, M. A. Pedrosa, R. Balbín, I. García-Cortés, B. van Milligen, D. E. Newman, and V. E. Lynch, "Fluctuation-induced flux at the plasma edge in toroidal devices," Phys. Plasmas **3**, 2664–2672 (1996).

[14]P. A. Politzer, "Observation of avalanchelike phenomena in a magnetically confined plasma," Phys. Rev. Lett. **84**, 1192–1195 (2000).

[15]E. Kim, P. Diamond, M. Malkov, T. Hahm, K. Itoh, S.-I. Itoh, S. Champeaux, I. Gruzinov, O. Gurcan, C. Holland, M. Rosenbluth, and A. Smolyakov, "Nonperturbative models of intermittency in drift-wave turbulence: Towards a probabilistic theory of anomalous transport," Nucl. Fusion **43**, 961 (2003).

[16]J. Anderson and P. Xanthopoulos, "Signature of a universal statistical description for drift-wave plasma turbulence," Phys. Plasmas **17**, 110702 (2010).

[17]E. Kim and J. Anderson, "Structure based statistical theory of intermittency," Phys. Plasmas **15**, 114506 (2008).

[18]E. Kim and P. H. Diamond, "Intermittency in drift-wave turbulence: Structure of the momentum flux probability distribution function," Phys. Rev. Lett. **88**, 225002 (2002).

[19]E. Kim and P. H. Diamond, "Zonal flows and transient dynamics of the L-H transition," Phys. Rev. Lett. **90**, 185006 (2003).

[20]M. A. Malkov and P. H. Diamond, "Weak hysteresis in a simplified model of the L-H transition," Phys. Plasmas **16**, 012504 (2009).

[21]H. Zhu, S. C. Chapman, and R. O. Dendy, "Robustness of predator-prey models for confinement regime transitions in fusion plasmas," Phys. Plasmas **20**, 042302 (2013).

[22]E. Kim and R. Hollerbach, "Time-dependent probability density functions and information geometry of the low-to-high confinement transition in fusion plasma," Phys. Rev. Res. **2**, 023077 (2020).

[23]R. Hollerbach, E. Kim, and L. Schmitz, "Time-dependent probability density functions and information diagnostics in forward and backward processes in a stochastic prey–predator model of fusion plasmas," Phys. Plasmas **27**, 102301 (2020).

[24]A. Newton, E. Kim, and H. Liu, "On the self-organizing process of large scale shear flows," Phys. Plasmas **20**, 092306 (2013).

[25]E. Kim, Q. Jacquet, and R. Hollerbach, "Information geometry in a reduced model of self-organised shear flows without the uniform coloured noise approximation," J. Statistical Mech.: Theory Experiment **2019**, 023204.

[26]J. W. Connor, "The neo-classical transport theory of a plasma with multiple ion species," Plasma Phys. **15**, 765 (1973).

[27]A. R. Field, J. McCone, N. J. Conway, M. Dunstan, S. Newton, and M. Wisse, "Comparison of measured poloidal rotation in MAST spherical tokamak plasmas with neo-classical predictions," Plasma Phys. Controlled Fusion **51**, 105002 (2009).

[28]H. Risken, *The Fokker-Planck Equation: Methods of Solutions and Applications* (Springer, 2013).

[29]E. Kim, "Information geometry and non-equilibrium thermodynamic relations in the over-damped stochastic processes," J. Statistical Mech.: Theory Experiment **2021**, 093406.

[30]E. Kim, "Information geometry, fluctuations, non-equilibrium thermodynamics, and geodesics in complex systems," Entropy **23**, 1393 (2021).

[31]B. R. Frieden, *Science from Fisher Information: A Unification* (Cambridge University Press, 2004).

[32]E. Solano, E. Delabie, G. Birkenmeier, C. Silva, J. Hillesheim, P. Vincenzi, A. Nielsen, J. Rasmussen, A. Baciero, S. Aleiferis, I. Balboa, A. Boboc, C. Bourdelle, I. Carvalho, P. Carvalho, M. Chernyshova, R. Coelho, T. Craciunescu, R. Dumont, P. Dumortier, E. la Luna, J. Flanagan, M. Fontana, J. Fontdecaba, L. Frassinetti, D. Gallart, J. Garcia, E. Giovannozzi, C. Giroud, W. Gromelski, R. Henriques, L. Horvath, P. Jacquet, I. Jepu, A. Kappatou, D. Keeling, D. King, E. Kowalska-Strzeciwilk, M. Lennholm, E. Lerche, E. Litherland-Smith, V. Kiptily, K. Kirov, A. Loarte, B. Lomanowski, C. Maggi, M. Mantsinen, A. Manzanares, M. Maslov, A. Meigs, I. Monakhov, R. Morales, D. Nina, C. Noble, V. Parail, F. Diaz, E. Pawelec, G. Pucella, D. Réfy, E. Righi-Steele, F. Rimini, T. Robinson, S. Saarelma, M. Sertoli, A. Shaw, S. Silburn, P. Sirén, Ž. Štancar, H. Sun, G. Szepesi, D. Taylor, E. Tholerus, S. Vartanian, G. Verdoolaege, B. Viola, H. Weisen, T. Wilson, and J. Contributors, "Recent progress in L-H transition studies at JET: Tritium, helium, hydrogen and deuterium," Nucl. Fusion **62**, 076026 (2022).